

Double Compton and Cyclo-Synchrotron in Super-Eddington Disks, Magnetized Coronae, and Jets

Jonathan C. McKinney^{1*}, Jens Chluba², Maciek Wielgus³, Ramesh Narayan⁴,
Aleksander Sadowski⁵,

¹University of Maryland at College Park, Dept. of Physics, Joint Space-Science Institute, 3114 Physical Sciences Complex, College Park, MD 20742, USA

²Jodrell Bank Centre for Astrophysics, University of Manchester, Oxford Road, Manchester M13 9PL, UK

³Copernicus Astronomical Center, ul. Bartycka 18, PL 00-716 Warszawa, Poland

⁴Harvard-Smithsonian Center for Astrophysics, 60 Garden St., Cambridge, MA 02134, USA

⁵MIT Kavli Institute for Astrophysics and Space Research, 77 Massachusetts Ave, Cambridge, MA 02139, USA

Accepted 2016. Received 2016; in original form 2016.

ABSTRACT

We present an extension to the general relativistic radiation magnetohydrodynamic code HARMRAD to account for emission and absorption by thermal cyclo-synchrotron, double Compton, bremsstrahlung, low-temperature OPAL opacities as well as Thomson and Compton scattering. We approximate the radiation field as a Bose-Einstein distribution and evolve it using the radiation number-energy-momentum conservation equations in order to track photon hardening. We perform various simulations to study how these extensions affect the radiative properties of magnetically-arrested disks accreting at Eddington to super-Eddington rates. We find that double Compton dominates bremsstrahlung in the disk within a radius of $r \sim 15r_g$ (gravitational radii) at a hundred times the Eddington accretion rate, and within smaller radii at lower accretion rates. Double Compton and cyclo-synchrotron regulate radiation and gas temperatures in the corona, while cyclo-synchrotron regulates temperatures in the jet. Interestingly, as the accretion rate drops to Eddington, an optically thin corona develops whose gas temperature of $T \sim 10^9$ K is ~ 100 times higher than the disk's black body temperature. Our results show the importance of double Compton and synchrotron in super-Eddington disks, magnetized coronae, and jets.

Key words: accretion, black hole physics, (magnetohydrodynamics) MHD, radiation

1 INTRODUCTION

Black hole (BH) accretion flows become radiation-dominated and geometrically thick once the luminosity $L \gtrsim 0.3L_{\text{Edd}}$, where $L_{\text{Edd}} \approx 1.3 \times 10^{46} [M/(10^8 M_\odot)] \text{ erg/s}$ is the Eddington luminosity for solar mass M_\odot and BH mass M . Such accretion flows tends to have temperatures of $10^9 \gtrsim T \gtrsim 10^6$ Kelvin (Abramowicz et al. 1988), where bremsstrahlung (free-free, $ep \rightarrow e'p'\gamma$) is important.

Double (radiative) Compton (DC, $\gamma_1 e \rightarrow \gamma_1' \gamma_2 e'$) (Lightman 1981; Thorne 1981; Pozdnyakov et al. 1983; Svensson 1984) can dominate free-free while regulating temperatures so that pairs remain sub-dominant (see figure 1 in Thorne 1981). While double Compton has received attention in cosmology to determine distortions to the cosmic microwave background (Chluba & Sunyaev 2012; Chluba 2014) and been applied to gamma-ray bursts (Vurm et al. 2013; Bégué & Pe'er 2015), it has received little attention in accretion theory except by Poutanen & Svensson (1996).

For photon number density n_γ , ion number density n_i , electron mass m_e , speed of light c , Boltzmann's constant k_b , and temperature T , the rates of each process show that DC dominates free-free if

$$\frac{n_\gamma}{n_i} \gtrsim 1.3 \left(\frac{m_e c^2}{k_b T} \right)^{5/2}, \quad (1)$$

(Thorne 1981; Svensson 1984), which has the correction by Svensson (1984) of 1.3 instead of the value 0.1 by Thorne (1981). In this paper, we find DC dominates free-free for the mean opacity when

$$T > 7 \times 10^7 \text{ K} \rho^{2/11} \quad (2)$$

where ρ is mass density in cgs units. For BH X-ray binaries accreting at ten times the Eddington rate, one has $\rho \approx 10^{-3} \text{ g cm}^{-3}$ giving equality at $T \approx 2 \times 10^7$ K, while simulations show that $T \sim 5 \times 10^7 - 10^8$ K (Sadowski & Narayan 2015a) indicating double Compton dominates free-free even if not yet included. For super-massive BHs relevant for tidal disruption events (TDEs) accreting at the Eddington rate, one has $\rho \sim 10^{-9} \text{ g cm}^{-3}$ giving equality at $T \approx 1.4 \times 10^6$ K, which is reached within tens of gravitational radii.

Still, it remains uncertain which opacity dominates the mean

* E-mail: jcm@umd.edu (JCM)

flow behavior. The Novikov-Thorne solution (Novikov & Thorne 1973) or slim disk solution (Abramowicz et al. 1988) could be used as a guide to how important DC is, but we find the temperature sensitivity makes the conclusions not robust – especially as the slim disk solution is modified by winds, vertical structure, and magnetic fields. Also, unlike free-free, double Compton is entirely dependent upon the radiation temperature for non-relativistic electrons, so non-local thermodynamic equilibrium (LTE) effects are important to treat. This motivates using simulations to consider both opacities with separate gas and radiation temperatures.

In addition, cyclo-synchrotron (hereafter, synchrotron) is expected to be an important source of opacity or emission for low-luminosity accretion flows or in regions where non-thermal electrons are present. In super-Eddington accretion flows, one expects synchrotron to be unimportant in the disk. However, the atmosphere above the disk (i.e. corona) and jet can contain a strong magnetic field at low densities where synchrotron can dominate (Di Matteo et al. 1997; Uzdensky & McKinney 2011). In addition, magnetically-arrested accretion disks (MADs) are much more strongly magnetized than weakly magnetized disks that are usually considered (Igumenshchev et al. 2003; Narayan et al. 2003; Tchekhovskoy et al. 2011). Magnetically-supported atmospheres can harden the spectrum by producing a more extended vertical disk (Blaes et al. 2006), and synchrotron can provide an abundant source of low-energy soft photons that can undergo inverse Compton before being absorbed. So the magnetic field strength can regulate photon hardening in disk atmospheres and magnetized jets.

In this paper, we consider the competition between free-free, bound-free, bound-bound opacities from OPAL (Iglesias & Rogers 1996), double Compton, and synchrotron in MAD type black hole accretion flows. We also consider separate absorption and emission mean opacities to focus on emission rates in the energy and momentum equations, rather than the Rosseland mean that only applies in the diffusion limit for the momentum equation. The absorption mean handles the effect of irradiation and how the absorption of radiation is affected by the photon distribution being different than that given by Planck at the local temperature (Sadowski et al. 2016). Such non-LTE effects lead to a significant correction to the mean opacities and can qualitatively change the outcome (Hubeny et al. 2003). Additionally, we evolve the photon number separately from the photon energy (Sadowski & Narayan 2015a), with separate number and energy opacities, in order to track photon hardening due to inverse Comptonization. The photon distribution is assumed to be Bose-Einstein, but with a low-energy transition to Planck when absorption is faster than inverse Compton.

These physical effects are included within our general relativistic (GR) radiative magnetohydrodynamics (MHD) (GR-RMHD) code HARMRAD (McKinney et al. 2014) that uses the M1 closure. Similar GR (Fragile et al. 2012; Takahashi et al. 2013; Sądowski et al. 2014; McKinney et al. 2014; Fragile et al. 2014; Ryan et al. 2015; Takahashi et al. 2016) and non-GR (Jiang et al. 2014a) schemes have been developed.

In §2, we outline our equations of motion, in §3 we present our GRRMHD simulations, and in §4 we summarize our results. For the appendices, in §A, we discuss our use of the Bose-Einstein distribution, in §B we discuss how we compute the mean opacities, in §C we discuss free-free and related low-temperature opacities, in §D we discuss synchrotron opacities, and in §E we discuss Compton scattering and double Compton opacities.

2 EQUATIONS OF MOTION

The conservation laws are

$$(\rho u^\mu)_{;\mu} = 0, \quad (3)$$

$$(T_v^\mu)_{;\mu} = G_v, \quad (4)$$

$$(R_v^\mu)_{;\mu} = -G_v, \quad (5)$$

where ρ is the gas density in the comoving fluid frame, u^μ is the gas four-velocity as measured in the “lab frame”, and T_v^μ is the MHD stress-energy tensor in this frame,

$$T_v^\mu = (\rho + u_g + p_g + b^2)u^\mu u_v + (p_g + \frac{1}{2}b^2)\delta_v^\mu - b^\mu b_v, \quad (6)$$

R^μ is the stress-energy tensor of radiation, G_v is the radiative four-force describing the interaction between gas and radiation, u_g and p_g are, respectively, the internal energy and pressure of the gas in the comoving frame, and b^μ is the magnetic field 4-vector (Gammie et al. 2003). The magnetic pressure is $p_b = b^2/2$ in our Heaviside-Lorentz units. The ideal induction equation and entropy equations are also used (McKinney et al. 2014). We assume collisions keep gas and electron temperatures similar (Sadowski et al. 2016).

2.1 Radiative four-force

We use a covariant formalism for computing the interaction due to absorption, emission, and scattering (Sądowski et al. 2014; McKinney et al. 2014) via a 4-force between the gas and radiation of

$$G^\mu = -(\kappa_a + \kappa_s)R^{\mu\nu}u_\nu - (\kappa_s R^{\alpha\beta}u_\alpha u_\beta + \lambda)u^\mu, \quad (7)$$

where κ_a is the energy absorption mean opacity in the fluid frame (in which ions and electrons are isotropic), λ is the fluid-frame total energy density loss rate before absorption (which includes changes in energy while conserving photon number), and κ_s is the fluid-frame energy scattering mean opacity.

2.2 Photon Number Evolution

If the radiation is Planckian, then the chemical potential $\mu = 0$ and the radiation temperature is derived from only the fluid-frame radiation energy density via $T_r = (E/a)^{1/4}$ where $E = R^{\mu\nu}u_\mu u_\nu$, which can differ from the gas temperature T_g or electron temperature T_e .

A more general photon distribution, like our choice of a Bose-Einstein distribution (see §A), can be considered by simultaneously evolving the number density of photons in the radiation frame (n_r , for radiation isotropic in the frame with 4-velocity u_r^μ) via

$$(n_r u_r^\mu)_{;\mu} = \dot{n}, \quad (8)$$

where the fluid-frame number density of photons is $n = n_r(-u_r^\mu u_\mu)$ and $\dot{n}_r = \dot{n}$ by Lorentz invariance, with

$$\dot{n} = -(\kappa_{na}c)n - \lambda_n, \quad (9)$$

for a number absorption mean opacity κ_{na} and total number emission rate λ_n before absorption. This photon number conservation equation approximates the Kompaneets equation most accurately when thermal Comptonization is included and when gas and radiation temperatures are similar (Sadowski & Narayan 2015a).

2.3 Opacities and Rates

We obtain fits to several different energy-weighted and number-weighted opacities (computed as in §B), including OPAL opacities

for solar abundances (energy mean $\kappa_{a,\text{eff}}$ and number mean $\kappa_{a,\text{eff}}$) in §C, synchrotron (energy mean $\kappa_{a,\text{syn}}$ and number mean $\kappa_{a,\text{syn}}$) in §D, and Compton scattering (scattering energy mean κ_s , thermal Comptonization energy exchange rate λ_c , and double Compton energy mean opacity $\kappa_{a,\text{dc}}$ and number mean opacity $\kappa_{a,\text{dc}}$) in §E.

Then, the energy mean energy absorption opacity is

$$\kappa_a = \kappa_{a,\text{eff}} + \kappa_{a,\text{syn}} + \kappa_{a,\text{dc}}, \quad (10)$$

and the number mean number absorption opacity is

$$\kappa_{an} = \kappa_{a,\text{eff}} + \kappa_{a,\text{syn}} + \kappa_{a,\text{dc}}. \quad (11)$$

From these opacities, the energy and number emission rates before any absorption are obtained in §B5, giving energy emission rate λ_e and number emission rate λ_n such that

$$\lambda = \lambda_e + \lambda_c, \quad (12)$$

and λ_n includes all number emission.

We do not include thermal pairs relevant when $k_b T_e \gtrsim m_e c^2$ as only the jet can be that hot and there one requires pair production (see, e.g., appendix B in McKinney & Uzdensky 2012).

3 SIMULATIONS

Our GRRMHD simulations evolve accretion flows around black holes with black hole mass of $M = 10M_\odot$. All models have identical initial conditions, except some have different initial density values due to an overall rescaling of the density in order to vary the final mass accretion rate \dot{M} . For different models, we vary the choices of opacity and how the temperature of radiation is evolved, and we investigate how the opacity and radiation temperature evolution affect the accretion flow behavior and properties.

3.1 Diagnostics

For various quantities R , we consider time-averages ($[R]_t$), spatial averages, and their spatial distributions. Diagnostics are computed from snapshots produced every $\sim 4r_g/c$ for $r_g \equiv GM/c^2$ with gravitational constant G .

3.1.1 Fluxes

The stress energy tensor T^μ_ν includes both matter (MA) and electromagnetic (EM) terms:

$$\begin{aligned} T^{\text{MA}\mu}_\nu &= (\rho + u_g + p_g)u^\mu u_\nu + p_g \delta^\mu_\nu, \\ T^{\text{EM}\mu}_\nu &= b^2 u^\mu u_\nu + p_b \delta^\mu_\nu - b^\mu b_\nu, \end{aligned} \quad (13)$$

Here, u_g is the internal energy density and $p_g = (\Gamma - 1)u_g$ is the ideal gas pressure with adiabatic index Γ . The contravariant fluid-frame magnetic 4-field is given by b^μ , which is related to the lab-frame 3-field via $b^\mu = B^r h^\mu_\nu / u^\nu$ where $h^\mu_\nu = u^\mu u_\nu + \delta^\mu_\nu$ is a projection tensor, and δ^μ_ν is the Kronecker delta function. The magnetic energy density (u_b) and pressure (p_b) are $u_b = p_b = b^\mu b_\mu / 2 = b^2 / 2$. The total pressure is $p_{\text{tot}} = p_g + p_b$, and plasma $\beta \equiv p_g / p_b$.

The gas rest-mass flux, specific energy flux, and specific an-

gular momentum flux are respectively given by

$$\dot{M} = \left| \int \rho u^r dA_{\theta\phi} \right|, \quad (14)$$

$$e \equiv \frac{\dot{E}}{[\dot{M}]_t} = - \frac{\int (T^r_t + R^r_t) dA_{\theta\phi}}{[\dot{M}]_t}, \quad (15)$$

$$j \equiv \frac{\dot{J}}{[\dot{M}]_t} = \frac{\int (T^r_\phi + R^r_\phi) dA_{\theta\phi}}{[\dot{M}]_t}, \quad (16)$$

where $dA_{\theta\phi} = \sqrt{-g} dx^{(2)} dx^{(3)}$ for metric determinant $g = \text{Det}(g_{\mu\nu})$ and uniform code coordinates with spacing $dx^{(1)}$, $dx^{(2)}$, and $dx^{(3)}$ in the radial-like, θ -like, and ϕ -like directions.

The net flow efficiency is given by

$$\eta = \frac{\dot{E} - \dot{M}}{[\dot{M}]_t}, \quad (17)$$

Positive values correspond to an extraction of positive energy from the system at some radius. The jet efficiency η_j includes all non-radiative terms in \dot{E} .

The magnetic flux is given in a normalized form as

$$\Upsilon_H \approx 0.7 \frac{\int 0.5 |B^r| dA_{\theta\phi}}{\sqrt{[\dot{M}]_t}}, \quad (18)$$

which accounts for B^r being in Heaviside-Lorentz units (Gammie 1999; Penna et al. 2010).

3.1.2 Inflow Equilibrium

Inflow equilibrium is defined as when the flow is in a complete quasi-steady-state and the accretion fluxes are constant (apart from noise) vs. radius and time. The inflow equilibrium timescale is

$$t_{\text{ie}} = N \int_{r_i}^{r_{\text{ic}}} dr \left(\frac{-1}{\langle v_r \rangle_\rho} \right), \quad (19)$$

where $\langle v_r \rangle_\rho$ is the ρ weighted radial velocity, and $N \sim 3$ inflow times from $r = r_{\text{ic}}$ and $r_i = 12r_g$.

Viscous theory gives a GR α -viscosity estimate for v_r of $v_{\text{visc}} \sim -Q\alpha(H/R)^2 |v_{\text{rot}}|$ for rotational velocity v_{rot} , disk thickness H/R , and GR correction Q (Page & Thorne 1974; Penna et al. 2010), so we can define an effective α viscosity as

$$\alpha_{\text{eff}} \equiv \frac{v_r}{v_{\text{visc}}/\alpha}. \quad (20)$$

All our models have $\alpha_{\text{eff}} \sim 1$ in the quasi-steady state, as expected for MADs (McKinney et al. 2012).

3.1.3 Optical Depth and Radiative Quantities

The scattering optical depth is computed as

$$\tau_{\text{sca}} \approx \int \kappa_s dl, \quad (21)$$

while the effective optical depth for absorption is computed as

$$\tau_{\text{eff}} \approx \int \sqrt{3\kappa_a(\kappa_s + \kappa_a)} dl. \quad (22)$$

For the radial direction, $dl = -f_\gamma dr$, $f_\gamma \approx u^r (1 - (v/c) \cos \theta)$, $(v/c) \approx 1 - 1/(u^r)^2$ (as valid at large radii), $\theta = 0$, and the integral is from $r_0 = 4000r_g$ to r to obtain $\tau_r(r)$. For the angular direction, $dl = f_\gamma r d\theta$, $\theta = \pi/2$, and the integral is from each polar axis toward the equator to obtain $\tau_\theta(\theta)$. Note that the photospheres in the polar

jet region are strongly determined by the numerical density floors assumed.

To scale $\dot{M}c^2$ or a luminosity L , one can use the Eddington luminosity

$$L_{\text{Edd}} = \frac{4\pi GMc}{\kappa_{\text{es}}} \approx 1.3 \times 10^{46} \frac{M}{10^8 M_{\odot}} \text{ erg s}^{-1}, \quad (23)$$

for Thomson electron scattering opacity κ_{es} . One can also choose to normalize \dot{M} by $\dot{M}_{\text{Edd}} = (1/\eta_{\text{NT}})L_{\text{Edd}}/c^2$, where η_{NT} is the nominal accretion efficiency for the Novikov-Thorne thin disk solution (Novikov & Thorne 1973) (commonly, a fixed $\eta_{\text{NT}} = 0.1$ is used, but we include the spin dependence).

The radiative luminosity is computed as

$$L_{\text{rad}} = - \int dA_{\theta\phi} R'_t, \quad (24)$$

which is measured just beyond the scattering photosphere to give the quantity we call $L_{\text{rad,o}}$. The radiative efficiency is $\eta_{\text{rad,o}} = L_{\text{rad,o}}/[M]_r$. From any cumulative luminosity $L(\theta)$, we can compute the isotropic equivalent luminosity

$$L_{\text{iso}}(\theta) = \pi \partial_{\theta} L(\theta) \quad (25)$$

and the corresponding beaming factor

$$b = \frac{L_{\text{iso}}}{L}. \quad (26)$$

The fluid-frame radiation temperature is

$$\hat{T}_{\gamma} \approx \frac{E}{n\bar{E}_0}, \quad (27)$$

with $\bar{E}_0 \approx 2.701k_{\text{B}}$, which is to within 10% of the full Bose-Einstein formula given by Eq. (A5) that we actually use. The lab-frame radiation temperature is

$$T_{\gamma} \approx \frac{-R'_t}{n_r u'_r \bar{E}_0}. \quad (28)$$

The black-body assumption gives a fluid-frame temperature of

$$\hat{T}_{\text{BB}} = \left(\frac{E}{a_{\text{rad}}} \right)^{1/4}, \quad (29)$$

for radiation constant a_{rad} , while in the lab-frame the assumption of Planck gives

$$T_{\text{BB}} = \left(\frac{-R'_t}{a_{\text{rad}}} \right)^{1/4}. \quad (30)$$

From these one can compute the lab-frame photon hardening factor

$$f_{\text{col}} = \frac{T_{\gamma}}{T_{\text{BB}}}, \quad (31)$$

and the fluid-frame hardening factor

$$\hat{f}_{\text{col}} = \frac{\hat{T}_{\gamma}}{\hat{T}_{\text{BB}}}. \quad (32)$$

3.1.4 Numerical Diagnostics

The magneto-rotational instability (MRI) is a linear instability with fastest growing wavelength of

$$\lambda_{x,\text{MRI}} \approx 2\pi \frac{|v_{x,A}|}{|\Omega_{\text{rot}}|}, \quad (33)$$

for $x = \theta, \phi$, where $|v_{x,A}| = \sqrt{b_x b^x / \epsilon}$ is the x -directed Alfvén speed, $\epsilon \equiv b^2 + \rho + u_g + p_g$, and $r\Omega_{\text{rot}} = v_{\text{rot}}$. Ω_{rot}, v_A are separately angle-volume-averaged at each r, t .

The MRI is resolved for grid cells per wavelength (Eq. (33)),

$$Q_{x,\text{MRI}} \equiv \frac{\lambda_{x,\text{MRI}}}{\Delta_x}, \quad (34)$$

of $Q_{x,\text{MRI}} \geq 6$, for $x = \theta, \phi$, where $\Delta_r \approx dx^{(1)}(dr/dx^{(1)})$, $\Delta_{\theta} \approx rd_x^{(2)}(d\theta/dx^{(2)})$, and $\Delta_{\phi} \approx r \sin \theta dx^{(3)}(d\phi/dx^{(3)})$. Volume-averaging is done as with $S_{d,\text{MRI}}$, except $v_{x,A}/\Delta_x$ and $|\Omega_{\text{rot}}|$ are separately θ, ϕ -volume-averaged before forming $Q_{x,\text{MRI}}$. At $t = 0$ all our models have $Q_{\theta,\text{MRI}} \sim 40$ and is constant all along the disk, while in a steady-state all our models have $Q_{\theta,\text{MRI}} \sim 100$ and $Q_{\phi,\text{MRI}} \sim 20$ (except model M13 that is quite thin and has $Q_{\phi,\text{MRI}} \sim 6$ and so probably has somewhat underdeveloped MRI turbulence).

The MRI suppression factor corresponds to the number of MRI wavelengths across the full disk:

$$S_{d,\text{MRI}} \equiv \frac{2r(H/R)}{\lambda_{\theta,\text{MRI}}}. \quad (35)$$

Wavelengths $\lambda < 0.5\lambda_{\theta,\text{MRI}}$ are stable, so the linear MRI is suppressed for $S_{d,\text{MRI}} < 1/2$ when no unstable wavelengths fit within the full disk (Balbus & Hawley 1998; Pessah & Psaltis 2005). $S_{d,\text{MRI}}$ uses averaging weight $w = (b^2\rho)^{1/2}$, condition $\beta > 1$, and excludes regions where density floors are activated. When computing the averaged $S_{d,\text{MRI}}$, v_A and $|\Omega_{\text{rot}}|$ are separately θ, ϕ -volume-averaged within $\pm 0.2r$ for each t, r . The $S_{d,\text{MRI}} \sim 0.5$ at $t = 0$, while in quasi-steady-state $S_{d,\text{MRI}} \sim 0.1$. So the field strength has increased considerably due to magnetic flux accumulation. All models are MAD with $S_{d,\text{MRI}} < 1/2$ out to $r \sim 30r_g$.

The flow structure can also be studied by computing the correlation length scale and then computing how many grid cells cover each self-correlated piece of turbulence. We follow our prior works McKinney et al. (2012) and McKinney et al. (2014) and compute this. One would desire to have at a minimum 6 grid cells per correlation length scale, since otherwise uncorrelated parts of turbulence are not independently resolved by our piece-wise parabolic monotonicity-preserving (PPM) scheme that needs 6 grid cells to resolve a structure well. All our models have ≈ 12 grid cells per vertical and radial correlation length for density and magnetic field strength, while our moderate resolution models have ≈ 6 cells in the ϕ -direction per correlation length scale. Our survey models have only ≈ 3 cells in the ϕ -direction per correlation length. This means the survey models should be considered not resolved enough to demonstrate fully resolved turbulence, but they are still sufficiently interesting to identify what physical effects (being switch on/off) could be important in fully resolved simulations. In addition, we compare some survey models against moderate resolution versions to confirm the survey models are reasonable.

3.2 Initial Conditions

The initial disk is Keplerian with a rest-mass density that is Gaussian in angle with a height-to-radius ratio of $H/R \approx 0.2$ and radially follows a power-law of $\rho \propto r^{-0.6}$. The solution near and inside the inner-most stable circular orbit (ISCO) is not an equilibrium, so near the ISCO the solution is tapered to a smaller density ($\rho \rightarrow \rho(r/15)^7$, within $r = 15r_g$) and a smaller thickness ($H/R \rightarrow 0.2(r/10)^{0.5}$, within $r = 10r_g$ – based upon a low-resolution simulation). The total internal energy density u_{tot} is estimated from vertical equilibrium of $H/R \approx c_s/v_K$ for sound speed $c_s \approx \sqrt{\Gamma_{\text{tot}} P_{\text{tot}}/\rho}$ with $\Gamma_{\text{tot}} \approx 4/3$ and Keplerian speed $v_K \approx (r/r_g)/((r/r_g)^{3/2} + a/M)$. The total ideal pressure $P_{\text{tot}} = (\Gamma_{\text{tot}} - 1)u_{\text{tot}}$ is randomly perturbed by 10% to seed the MRI. The disk gas has $\Gamma_{\text{gas}} = 5/3$. The disk has an atmosphere with $\rho = 10^{-5}(r/r_g)^{-1.1}$ and gas internal energy density

Table 1. Spin, Mass Accretion Rate, Opacity, and Temperature Choices

Model	a/M	$\frac{\dot{M}_H}{\dot{M}_{\text{Edd}}}$	Opacities	Radiation Number Density	Radiation Temperature	Chemical Potential
M1	0.8	140	OPAL+Syn+DC	Evolved	$E/(n\bar{E}_0)$	1
M2	0.8	140	OPAL	Evolved	$E/(n\bar{E}_0)$	1
M3	0.8	80	OPAL	Evolved	Bose-Einstein	Bose-Einstein
M5	0.8	120	OPAL	Planck at \hat{T}_γ	Planck at \hat{T}_γ	1
M6	0	5.9	OPAL (no TC)	Planck at \hat{T}_γ	Planck at \hat{T}_γ	1
M7	0	4.8	OPAL	Evolved	$E/(n\bar{E}_0)$	1
M8	0	5	OPAL+Syn+DC	Evolved	$E/(n\bar{E}_0)$	1
M9	0.8	50	OPAL+Syn+DC	Evolved	Bose-Einstein	Bose-Einstein
M10	0.8	27	OPAL+DC	Evolved	Bose-Einstein	Bose-Einstein
M11	0.8	36	OPAL+Syn+DC	Evolved	Bose-Einstein	Bose-Einstein
M13	0.8	1.2	OPAL+Syn+DC	Evolved	Bose-Einstein	Bose-Einstein
M14	0.8	3.5	OPAL+Syn+DC	Evolved	Bose-Einstein	Bose-Einstein
M14h	0.8	2.4	OPAL+Syn+DC	Evolved	Bose-Einstein	Bose-Einstein
M15	0.8	14	OPAL+Syn+DC	Evolved	Bose-Einstein	Bose-Einstein
M15h	0.8	31	OPAL+Syn+DC	Evolved	Bose-Einstein	Bose-Einstein

$u_g = 10^{-6}(r/r_g)^{-5/2}$. The disk's radiation energy density and flux are set by LTE and flux-limited diffusion (McKinney et al. 2014).

The initial magnetic field is large-scale and poloidal. For $r < 300r_g$, the coordinate basis ϕ -component of the vector potential is

$$A_\phi = \text{MAX}(r^\nu 10^{40} - 0.02, 0)(\sin \theta)^{1+h}, \quad (36)$$

with $\nu = 0.75$ and $h = 4$. For $r \geq r_0 = 300r_g$, the field transitions to monopolar using $A_\phi = \text{MAX}(r_0^\nu 10^{40} - 0.02, 0)(\sin \theta)^{1+h(r_0/r)}$. The field is normalized with ~ 1 MRI wavelength per half-height H giving a ratio of average gas+radiation pressure to average magnetic pressure of $\beta \approx 40$ for $r < 100r_g$.

3.3 Numerical Setup

The numerical grid mapping equations and boundary conditions used here are identical to that given in McKinney et al. (2012) and McKinney et al. (2014). The grid focuses on the disk at small radii and on the jet at large radii.

Models M14h and M15h are moderate resolution models at $N_r \times N_\theta \times N_\phi = 128 \times 64 \times 64$, while the rest are survey models at $128 \times 64 \times 32$ in order to resolve the lowest order m modes to allow for accretion in MADs. For MADs such lower resolution models have shown reasonable convergence (McKinney et al. 2012, 2014). The grid aspect ratio is roughly 1:1:1 for radii $5r_g \leq r \leq 30r_g$ for our moderate resolution models.

The rest-mass and internal energy densities are driven to zero near the BH within the jet and near the axis, so we use numerical ceilings of $b^2/\rho = 300$, $b^2/u_g = 10^{11}$, and $u_g/\rho = 10^{10}$. The value of b^2/ρ is at the code's robustness limit for the chosen resolution, while the value of b^2/u_g is chosen to ensure an artificial temperature floor is not introduced.

At early times in all simulations, we ramp-up the chemical potential factor from Planck toward its desired target. This avoids difficult-to-resolve opacity changes due to synchrotron within the first $100r_g/c$ in time. Also, the sharp changes in synchrotron opacity for high ϕ (Eq. D5) near Planck (i.e. $\exp(-\xi) = 1$ with dimensionless chemical potential $\xi = 0$) are difficult to handle. For synchrotron only, we enforce $\exp(-\xi) \leq 0.99$ in order to smooth-out these opacity changes (Seaton 1993).

3.4 Models

Our goal is to consider the physical effect of various choices for the radiative transfer opacities. We simulate several low-resolution "survey" runs over a time period of about $10000r_g/c$, allowing the simulations to reach a single inflow time out to $r \sim 50r_g$ and inflow equilibrium out to $r \sim 20r_g$. We check these survey runs with a couple moderate resolution runs, and we consider even lower resolution runs to see if resolution plays a dominate or sub-dominant role compared to the opacity effects.

Table 1 shows the physical choices made for each model, including the black hole spin, choices for opacities, whether the radiation photon number density is evolved, how the radiation temperature is computed, and whether the chemical potential is varied.

The "OPAL" opacity refers to the opacity κ_{eff} given by Eq. (C16). This is physically equivalent to the OPAL-based opacity used in Jiang et al. (2016), except ours is more approximate, but we also account for radiation temperatures being different from gas temperatures. "DC" refers to double Compton, which no simulations have yet accounted for. "Syn" refers to synchrotron, which has been accounted for in sub-Eddington accretion cases (Fragile & Meier 2009; Ryan et al. 2015; Sądowski et al. 2016). All models with photon number evolution include a separately-computed number mean opacity not yet accounted for in simulations (except only synchrotron number opacity in Sądowski et al. 2016). The simplified fluid-frame radiation temperature given by $\hat{E}/(\hat{n}\bar{E}_0)$ with $\bar{E}_0 \approx 2.701k_B$ is the dominant factor in Eq. (A5) (Sądowski & Narayan 2015a). We consider both Planck and Bose-Einstein photon distributions.

All models include thermal Comptonization (TC) except model M6 in order to study how turning that off affects gas temperatures. Model M6 would be like many existing radiative transfer simulations (Fragile et al. 2012; Jiang et al. 2014a; Fragile et al. 2014; Takahashi et al. 2016) except those by Fragile & Meier (2009); Kawashima et al. (2009); Jiang et al. (2014b) and ourselves (Sądowski et al. 2014; McKinney et al. 2014).

Models M9, M11, M12, M13, M14, M14h, M15, M15h are used to explore how varying \dot{M} affects the results while using our full opacity physics, with M9 and M11 not behaving much differently due to having similar \dot{M} .

Models M4 and M12 are very low resolution ($128 \times 64 \times 16$) test models that otherwise match models M3 and M11, respectively.

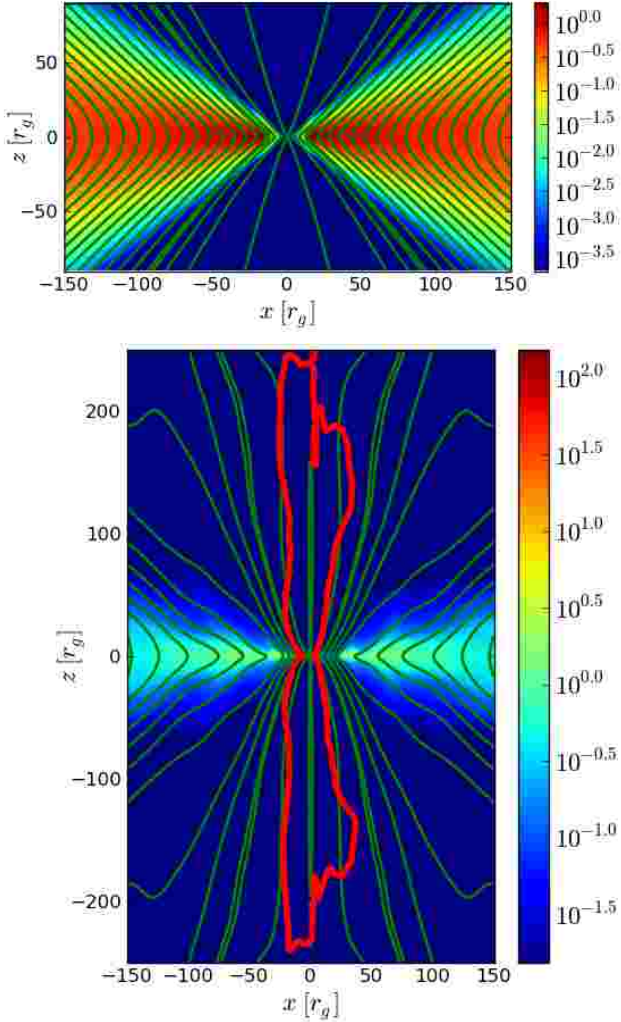


Figure 1. Model M15, showing the initial condition (top panel) and final state (bottom panel). The initial disk is shown as rest-mass density (scaled by an Eddington density value inferred from \dot{M}_{Edd} , r_g , and c , color with legend) threaded by magnetic field lines (green lines). The final disk has become much higher density near the black hole and the rotating black hole and disk have launched a magnetically-dominated jet due to the accumulation of magnetic flux into the MAD state. The BH-spin-driven jet emerges and has a boundary that can be seen where $b^2/\rho = 1$ (red line). At large radii at late time, the jet has become kinetically-dominated with Lorentz factor $\gamma \sim 2$ by $r = 500r_g$, so that $b^2/\rho < 1$ there.

These models and others at different resolutions exhibit all of the same radiative properties we will discuss, which shows that resolution is unlikely a dominant factor in the controlling our results. We do not discuss models M4 and M12 further.

Throughout our discussion of model results, we focus on specific models, often showing more details for model M15 because it has an intermediate mass accretion rate and demonstrates properties of all our models.

3.5 Initial and Final State

Fig. 1 shows the initial and final state of the accretion flow for model M15, which is typical of all models with rotating black holes. The initial magnetic field structure is large-scale and poloidal and threads the disk that is initially a Gaussian disk with $H/R \approx 0.2$

Table 2. Accretion Rates, Luminosities, Efficiencies [%], and Magnetic Fluxes

Model	$\frac{\dot{M}_H}{\dot{M}_{\text{Edd}}}$	$\frac{L_{\text{rad,o}}}{L_{\text{Edd}}}$	η_H	$\eta_{\text{j,in}}$	$\eta_{\text{o}}^{\text{RAD}}$	η_{NT}	Υ_H
M1	140	67	54.7	30.3	5.68	12.2	9.8
M2	140	110	58.3	40.7	9.76	12.2	9
M3	80	81	114	84.6	12.3	12.2	13
M5	120	81	59.2	36.3	8.39	12.2	9.5
M6	5.9	6	9.83	4.24	5.86	5.72	3.9
M7	4.8	2.4	7.98	0.926	2.84	5.72	3.9
M8	5	1.9	8.39	0.979	2.21	5.72	5
M9	50	240	124	71.6	59.4	12.2	14
M10	27	160	267	184	71.8	12.2	20
M11	36	290	185	110	95.5	12.2	18
M13	1.2	1.1	18.5	8.2	10.7	12.2	3.6
M14	3.5	2.8	23.7	11.4	9.79	12.2	5.1
M14h	2.4	2.5	21.8	11.3	12.7	12.2	4.7
M15	14	18	32.3	14.2	15.6	12.2	6.7
M15h	31	11	30.9	17.7	4.57	12.2	7.1

and a power-law radial behavior. The rotating black hole and disk have launched a jet that starts out magnetically-dominated but converts its energy into kinetic energy at large radii.

Table 2 shows results for dynamical quantities (like fluxes and efficiencies) for all our models as time-averaged from $4000r_g/c$ till the end of the simulation. This table can be used to compare results for models with different opacity physics and different \dot{M} . The models vary in mass accretion rate through the horizon with $\dot{M}/\dot{M}_{\text{Edd}} = 1\text{--}140$, and the radiative luminosity is given by $L_{\text{rad,o}}$. Other quantities are measured on the horizon (e.g. η_H), at an inner radius of $10r_g$ for inner ('i') quantities, or at large radii for outer ('o') quantities.

The efficiency η_H is the total efficiency of the system as measured at the horizon, which is constant to within 30% out to the scattering photosphere where outer quantities are measured. The total and radiative efficiency at large radii ($\eta_{\text{RAD,o}}$) are comparable to the NT standard thin disk efficiencies (η_{NT}). The total non-radiative jet efficiency $\eta_{\text{j,in}}$ is the efficiency at $r = 10r_g$ in the jet with $b^2/\rho > 1$. This tracks each model's total efficiency, but the jet energy is progressively lost to the surrounding material that heats-up and radiates (McKinney et al. 2015), leading to relatively low gas jet efficiencies by $r = 1000r_g$. The total radiative efficiency is therefore dependent upon the mass-loading physics, which is controlled partially by numerical floor injection in our simulations. For non-rotating BH models, the jet efficiency is low at 1%, except for the model without thermal Comptonization with jet efficiency at 4% due to the thermal energy content of the jet (this also leads to a slightly higher radiative efficiency).

The normalized magnetic flux on the horizon $\Upsilon_H \sim 10$ for relatively thick disks at higher super-Eddington rates, while lower \dot{M} lead to down to $\Upsilon_H \sim 4$ as seen in thin MAD simulations (Avara et al. 2015). A few models (M9, M10, and M11) show up to $\Upsilon_H \sim 20$ and have quite high efficiencies as apparently due to radiative suppression of the magnetic Rayleigh-Taylor modes due to opacity effects at their intermediate $\dot{M}/\dot{M}_{\text{Edd}} \sim 30\text{--}50$, but one suspects that higher resolutions would show no such effect (which M15h approaches and does show more moderate Υ_H and efficiencies).

Fig. 2 shows a snapshot from the simulation and shows various fluxes and efficiencies vs. time, whose constancy indicates that the flow has reached a quasi-steady state in which the total efficiency is $\eta_H \sim 30\%$, almost three times the NT thin disk efficiency and the

radiative efficiency is $\eta_{\text{rad,o}} \sim 5\%$. The disk is in a MAD state out to about $r \sim 50r_g$ with evident magnetic Rayleigh-Taylor instabilities in the $y-x$ plane. The dimensionless magnetic flux $\Upsilon \approx 7$, comparable with non-radiative disks with $H/R \approx 0.3$ (McKinney et al. 2012). The effective photosphere reaches close to the disk, except where the jet has relatively high densities.

Table 3 shows results for our radiative diagnostics, which can be used to deduce how the radiative properties are affected by different opacity choices and different \dot{M} . This table includes the fluid-frame radiation temperature per unit gas temperature at $r = 10r_g$ in the disk, fluid-frame radiation temperature in the disk, lab-frame radiation temperature in the radiation beam at $r = 100r_g$, fluid-frame hardening factor \hat{f}_{col} in the disk, lab-frame hardening factor f_{col} in the radiation beam at $r = 100r_g$, chemical potential factors in the disk and radiation beam, radiation beam half-opening angle (θ_r) at $r = 1000r_g$, and jet (kinetic+enthalpy+electromagnetic) half-opening angle (θ_j) at $r = 1000r_g$. Disk quantities are computed as weighted by volume of the grid cell times square of density, while radiation or electromagnetic beam quantities are measured at the peak in the luminosity per unit angle ($\partial_\theta L(\theta)$).

The low $\dot{M} \sim \dot{M}_{\text{Edd}}$ models have higher gas temperatures in the disk, but gas temperatures are at most about 10 times the radiation temperatures with thermal Comptonization. Only model M6 without thermal Comptonization shows very low \hat{T}_y/T_{gas} . The radiation beam and disk have hardening with a Wien spectrum in models without double Compton or in models with $\dot{M} \sim \dot{M}_{\text{Edd}}$.

The photon distributions tend to be somewhat Wien in the coronae for models with chemical potential evolution. Models without double Compton and synchrotron (like M2, M3, and M7) show significant photon hardening, which becomes much more limited when including these opacities. Radiation beam lab-frame temperatures are comparable to the disk core, except for models without double Compton and synchrotron. Models without double Compton and synchrotron (e.g. M7) have much higher radiation temperatures than otherwise identical models (e.g. M8) with double Compton and synchrotron. This shows that double Compton and synchrotron are crucial to include in order to obtain accurate observer-frame radiation temperatures for flows with $\dot{M} \gtrsim \dot{M}_{\text{Edd}}$.

The half-opening angles in radians identify the maximum in L_{iso} within the radiation beam or gas jet. We also computed (not in table) the beaming factor ($b = L_{\text{iso}}/L$, i.e. isotropic equivalent luminosity per unit total luminosity) measured at $r = 1000r_g$. The electromagnetic jet is beamed by factors up to $b = 10$ for rotating black hole models and up to $b = 5$ for non-rotating black hole models. The radiation beaming factor is up to $b = 8$ for rotating black hole models and $b = 3$ for non-rotating black hole models (similar to seen in Sadowski & Narayan 2015b). This corresponds to an enhanced radiative flux at specific viewing angles, with higher beaming for higher \dot{M} and higher a/M . The M1 closure slightly overestimates the beaming factors (Narayan et al. 2016).

3.6 Magnetic and Radiative Fluxes

Fig. 3 shows the magnetic flux lines (with electromagnetic efficiency) and lab-frame radiation flux stream lines (with radiative efficiency). The radiation is broadly distributed, but has an enhanced beamed region that sits in angle at about twice larger angle compared to the electromagnetic jet. Models with zero black hole spin (not plotted) show the peak EM luminosity per unit angle emerging from cylindrical radius near the ISCO (Tchekhovskoy et al. 2012), instead of the rotating black hole models where the peak power per unit angle emerges from near the equatorial region of the black hole

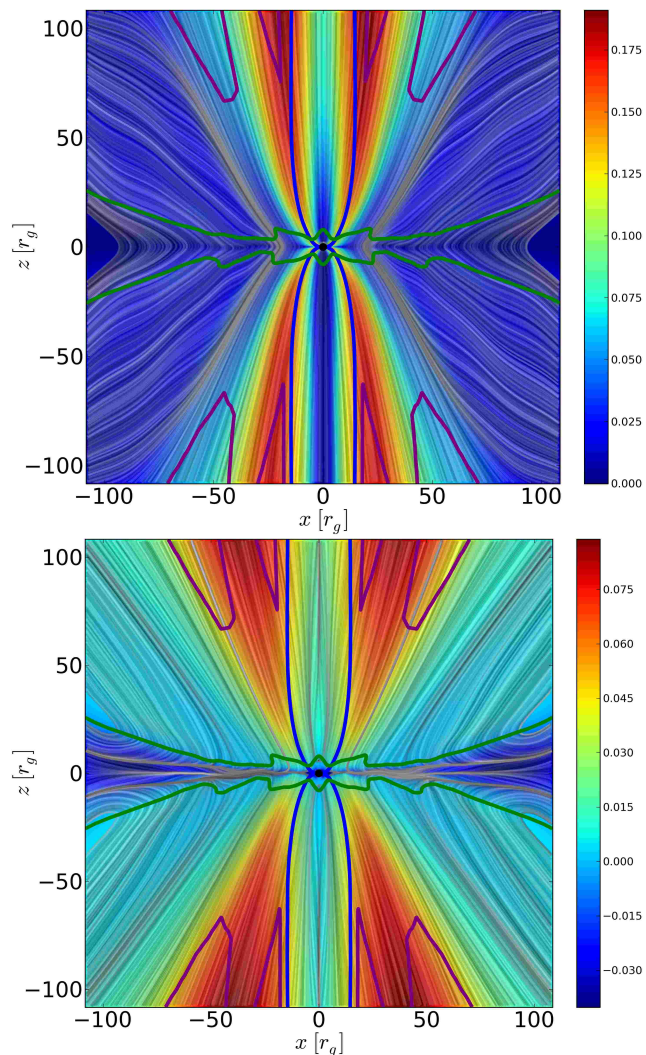


Figure 3. Model M15, with top panel showing time- ϕ -averaged magnetic flux lines (translucent gray lines) with electromagnetic luminosity per unit angle $(\partial_\theta L_{\text{EM}})/(\dot{M}Hc^2)$ (color with legend), with blue line showing where $b^2/\rho = 1$, green line showing where $u^t = 0$, and purple line showing total effective photosphere. Image is duplicated across the $x = 0$ line. The bottom panel shows same things for lab-frame radiation flux lines and radiation luminosity. The electromagnetic energy flux acts as a funnel-wall jet by following (and sitting just outside) the boundary where $b^2/\rho = 1$. Most of the electromagnetic energy is released from the black hole’s spin energy. The MAD equatorial region is quite hot and dynamic, leading to radiation emerging from quite close to the BH (and in a time-averaged sense, some appears to emerge from above the BH due to transient but powerful polar magnetic fields that jump between the BH and disk). Radiation moves inward within the disk that accumulates more radiative energy, which somewhat follows the path of the wind and ultimately becomes more radially-directed at larger distances.

horizon (McKinney & Gammie 2004; McKinney 2006; McKinney & Blandford 2009).

3.7 Effective Energy Photospheres

Fig. 4 shows the effective photospheres for model M15. At large radii, the total effective photosphere sits above the disk and disk wind. Sitting inside the total effective photosphere is the free-free photosphere, the double Compton photosphere, and the syn-

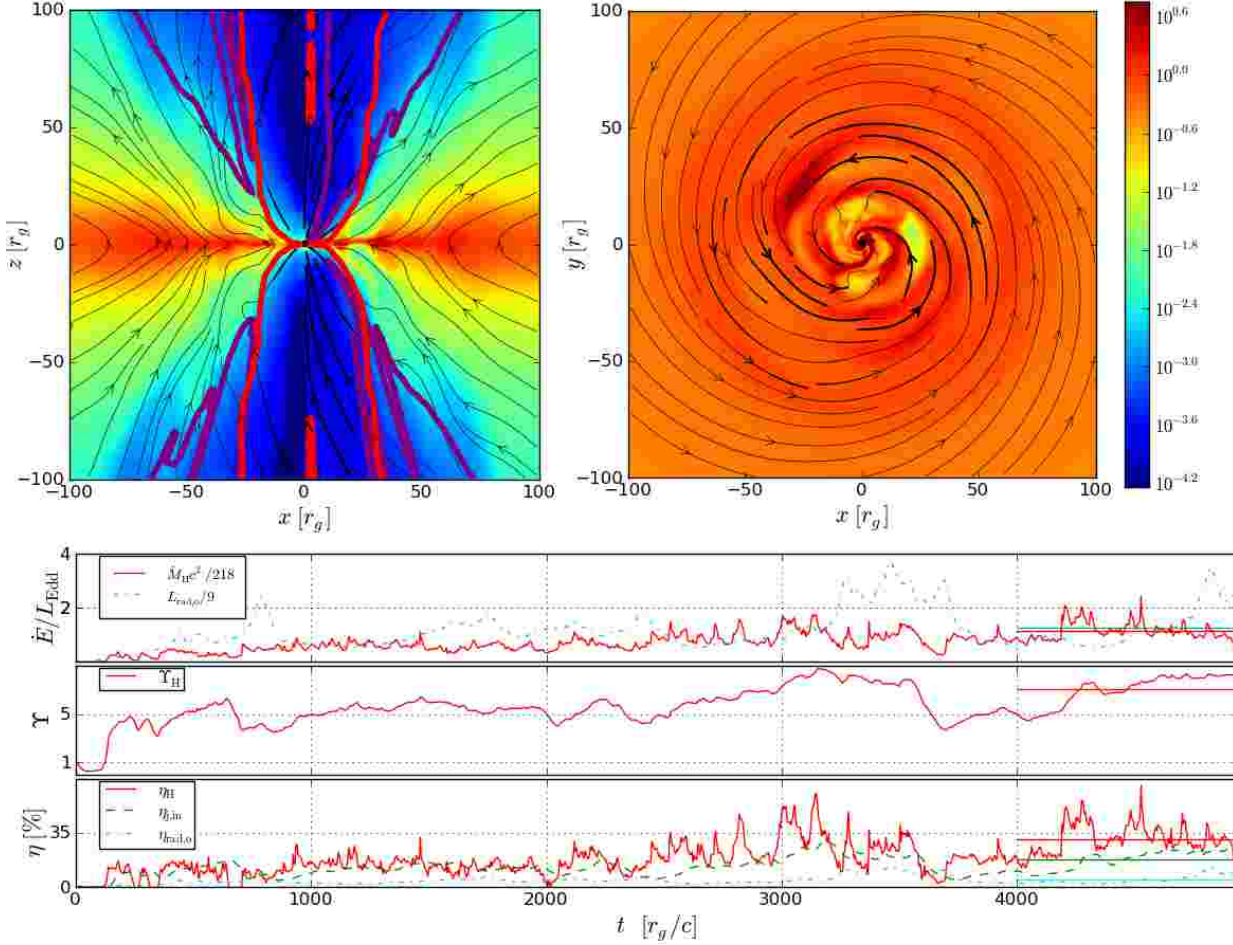


Figure 2. Evolved snapshot of model M15h at $t \approx 5000r_g/c$ showing log of rest-mass density (scaled by an Eddington density inferred from \dot{M}_{Edd} , r_g , and c , shown in color with legend on right) in both the $z-x$ plane at $y=0$ (top-left panel) and $y-x$ plane at $z=0$ (top-right panel). Black lines trace field lines. In the top-left panel, the thick red line corresponds to where $b^2/\rho = 1$ and the purple line corresponds to the effective photosphere (computed radially inward). The bottom panel has 3 subpanels. The top subpanel shows \dot{M} through the BH (\dot{M}_H) and radiative luminosity ($L_{\text{rad},o}$). The middle subpanel shows the magnetic flux passing through the horizon (Υ_H). The bottom subpanel shows the total efficiency (η_H), inner jet efficiency ($\eta_{j,\text{in}}$), and radiative efficiency ($\eta_{\text{rad},o}$). Horizontal solid lines of the same colors show the averages over the averaging period. For super-Eddington accretion at $\dot{M}/\dot{M}_{\text{Edd}} \approx 31$, the total BH efficiency is moderate at $\eta_H \approx 31\%$ with radiative efficiency of $\eta_{\text{rad},o} \approx 5\%$.

Table 3. Non-LTE and non-Planck Radiative Properties and Radiation/Jet Opening Angles in Radians

Model	$\left(\frac{\hat{T}_\gamma}{T_{\text{gas}}}\right)_{r=10r_g}$	$\hat{T}_{\gamma,r=10r_g}$ [K]	$T_{\gamma,r=100r_g,\text{rad.beam}}$ [K]	$f_{\text{col}}^{r=10r_g,\text{disk}}$	$f_{\text{col}}^{r=100r_g,\text{rad.beam}}$	$e_{r=10r_g,\text{disk}}^{-\xi}$	$e_{r=100r_g,\text{rad.beam}}^{-\xi}$	$\theta_r^{r=1000r_g}$	$\theta_j^{r=1000r_g}$
M1	0.96	4.2e7	1.7e7	1	1.4	1	1	0.12	0.067
M2	0.93	1.3e8	7.7e8	3.9	55	1	1	0.089	0.0038
M3	1	1.1e8	6e8	3.2	42	0.88	0.36	0.084	0.021
M5	0.97	3.8e7	9.1e6	1	0.77	1	1	0.092	0.025
M6	9.8e-5	1.5e7	3.3e6	1	0.58	1	1	0.6	0.12
M7	0.87	1.4e8	2.5e7	8.9	5.4	1	1	0.6	0.19
M8	0.63	1.9e7	6.7e6	1.1	1.6	1	1	0.6	0.15
M9	0.98	4.1e7	1.5e7	1	1.1	0.97	0.96	0.13	0.16
M10	0.99	4.9e7	2.1e7	1.3	1.6	0.87	0.69	0.13	0.041
M11	0.99	4.3e7	1.5e7	1	1	0.99	0.97	0.098	0.21
M13	0.12	3e7	9.2e6	4.5	2.6	0.43	0.45	0.28	0.0091
M14	0.23	1.5e7	2.1e6	1.3	0.48	0.79	0.94	0.26	0.011
M14h	0.2	1.3e7	2e6	1.2	0.45	0.76	0.99	0.47	0.055
M15	0.85	2.4e7	7.3e6	1.1	1.2	0.86	0.76	0.16	0.028
M15h	0.97	2.5e7	7.2e6	1	1.1	0.99	0.92	0.37	0.097

chrotron photosphere. The free-free, double Compton, and synchrotron opacities all merge within some radius, showing they become comparably important. While free-free and DC are clearly important in metal-free plasmas, bound-free and bound-bound contributions are important with solar abundances, which leads to an effective photosphere far beyond the free-free photosphere. For higher \dot{M} models, these different opacities become more comparable at larger radii than in this lower \dot{M} model. The scattering photosphere is at $r \sim 800r_g$ in this model.

3.8 Gas Over-Heated Regions

Fig. 5 shows the lab-frame radiation temperature and fluid-frame gas temperature for model M15. The radiation temperature reaches up to $T_\gamma \sim 10^8\text{K}$, while the gas temperature reaches up to $T_{\text{gas}} \sim 10^9\text{K}$ in the jet region. Given our discussion in the introduction, this suggests that double Compton should be important throughout the flow, while synchrotron is likely important in the jet region. Notice that as \dot{M} drops that the disk becomes thinner, although such MAD type disks are also magnetically-compressed by the large-scale poloidal and toroidal fields threading the black hole and disk (McKinney et al. 2012).

Fig. 6 shows the fluid-frame radiation temperature per unit gas temperature. Thermal Comptonization acts to regulate gas temperatures toward the radiation temperature in radiation-dominated plasmas. We show several model's poloidal plane temperature ratio in order to present how this effect works at high $\dot{M} \sim 100\dot{M}_{\text{Edd}}$ to low $\dot{M} \sim 1\dot{M}_{\text{Edd}}$. Notice that model M14 has a long-lived hemispherical asymmetry, leading to scattering photosphere far away on the upper hemisphere. The figure shows fluid-frame $\hat{T}_\gamma/T_{\text{gas}}$ (numerator and denominator separately time- ϕ -averaged). While lower \dot{M} models have a slightly over-heated gas region within some radius, the core disk region has at most 10% higher gas temperatures than radiation temperatures for $\dot{M} \sim 10\dot{M}_{\text{Edd}}$ models.

Model M13 with $\dot{M} \approx 1\dot{M}_{\text{Edd}}$ shows an optically thin corona with gas temperatures about 100 times larger than the disk's black body temperature and about 20 times larger than the disk's radiation temperature that is hardened by $f_{\text{col}} \approx 4.5$ (see related data from Fig. 9). The gas pressure is up to a tenth of the radiation pressure and the disk thickness $H/R \sim 0.1$ in this model.

Table 3 includes a sequence of $a/M = 0$ models M6, M7, and M8 which have no thermal Comptonization and no photon hardening (M6), have thermal Comptonization and photon hardening but without double Compton or synchrotron (M7), and have both along with all our opacities (M8). This shows that the lack of thermal Comptonization leads to unphysically high gas temperatures similar to seen in Takahashi et al. (2016), who did not include thermal Comptonization. Hence, thermal Comptonization is required for Eddington to super-Eddington accretion models.

3.9 Photon Hardening

Fig. 7 shows the lab-frame photon hardening factor ($f_{\text{col}} = T_\gamma/T_{\text{BB}}$) for the $a/M = 0$ models M6, M7, and M8 that we discussed above. For an observer in the lab-frame, this would correspond to the color correction factor assuming the observers fit spectra with Planck or BE distributions. We find that double Compton and synchrotron play a crucial role in limiting photon hardening. These opacities generate much more radiation at high temperatures, unlike free-free, and result in the primary radiation beam changing from $f_{\text{col}} = 5$ down to $f_{\text{col}} = 1.5$. Our model M7 is similar to the

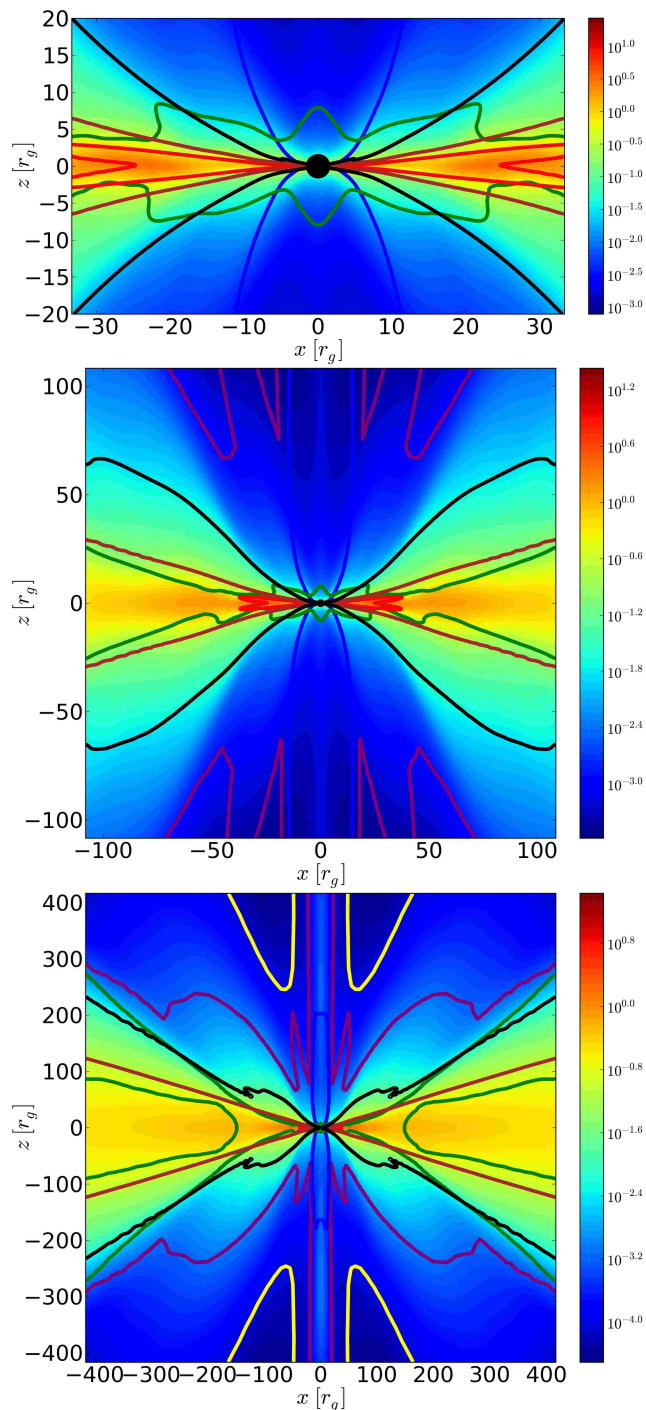


Figure 4. Model M15, showing effective photospheres for different processes, including OPAL+DC+synchrotron (purple line), synchrotron (red line), DC (brown line), free-free (black line), scattering only (yellow line) on different size regions (top, middle, bottom panels). The photospheres are computed radially inward from $r = 4000r_g$. Rest-mass density shown in color (with legend), scaled by an Eddington density value inferred from \dot{M}_{Edd} , r_g , and c . Green, blue, yellow, and purple lines are, if present, as in Fig. 3. For $r \lesssim 5r_g$, DC and free-free become comparably important processes in the disk. The effective photosphere somewhat follows the transition between disk inflow and wind outflow. The polar axis regions contains a high-density portion of the jet (launched by mass injection near the black hole) which leads to higher opacities there.

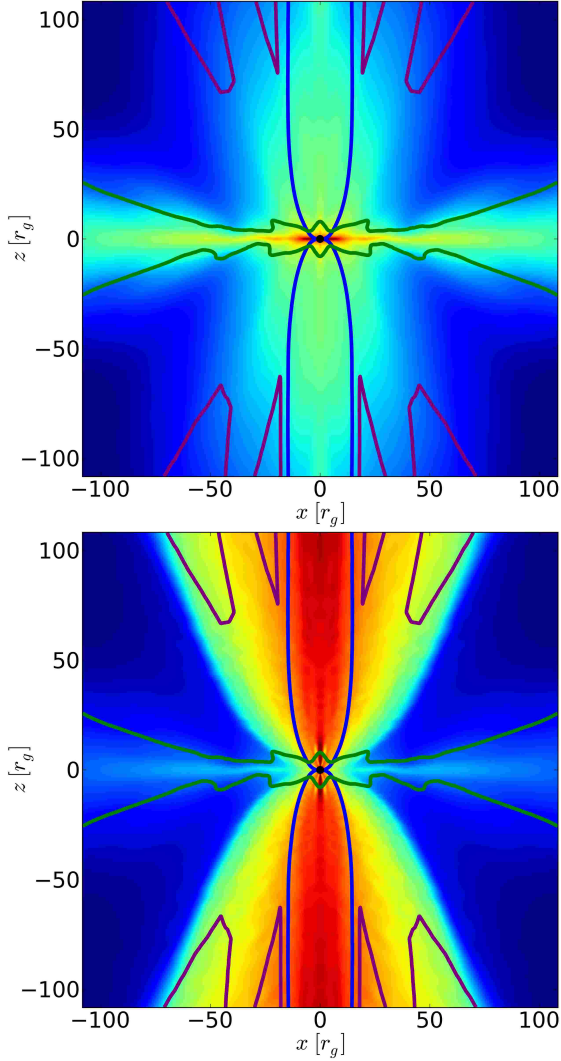


Figure 5. Model M15, showing lab-frame radiation temperature in Kelvin (top panel) and fluid-frame gas temperature in Kelvin (bottom panel). Green, blue, yellow, and purple lines are, if present, as in Fig. 3. Radiation temperatures are high in the equatorial and polar regions, while gas temperatures are high in the jet region due to insufficient Comptonization.

model in Sadowski & Narayan (2015a), who find up to $f_{\text{col}} = 7$ for comparable, but slightly higher, accretion rates. This shows that photon hardening in Eddington to super-Eddington flows must account for these additional opacities.

Table 3 shows \hat{f}_{col} in the disk and f_{col} in the jet for other models. These other models have a similar distribution for f_{col} vs. radius and angle as model M8 for models with double Compton and synchrotron or as model M7 for models without these processes. As $\dot{M} \rightarrow 1\dot{M}_{\text{Edd}}$, the photon hardening becomes stronger, a trend seen in AGN (Steffen et al. 2006; Just et al. 2007).

Table 3 includes two models, M10 and M11, where M10 has no synchrotron while M11 has all our opacities. These models have comparable \dot{M} and fluxes as shown in Table 2. The goal here is to see if double Compton by itself regulates photon hardening and to what extent synchrotron goes beyond double Compton. In model M10, the radiation beam is only moderately hardened due to the sensitivity of double Compton to radiation temperature, and synchrotron in M11 provides soft photons that lead to essentially no hardening of the radiation beam. This means double Compton by

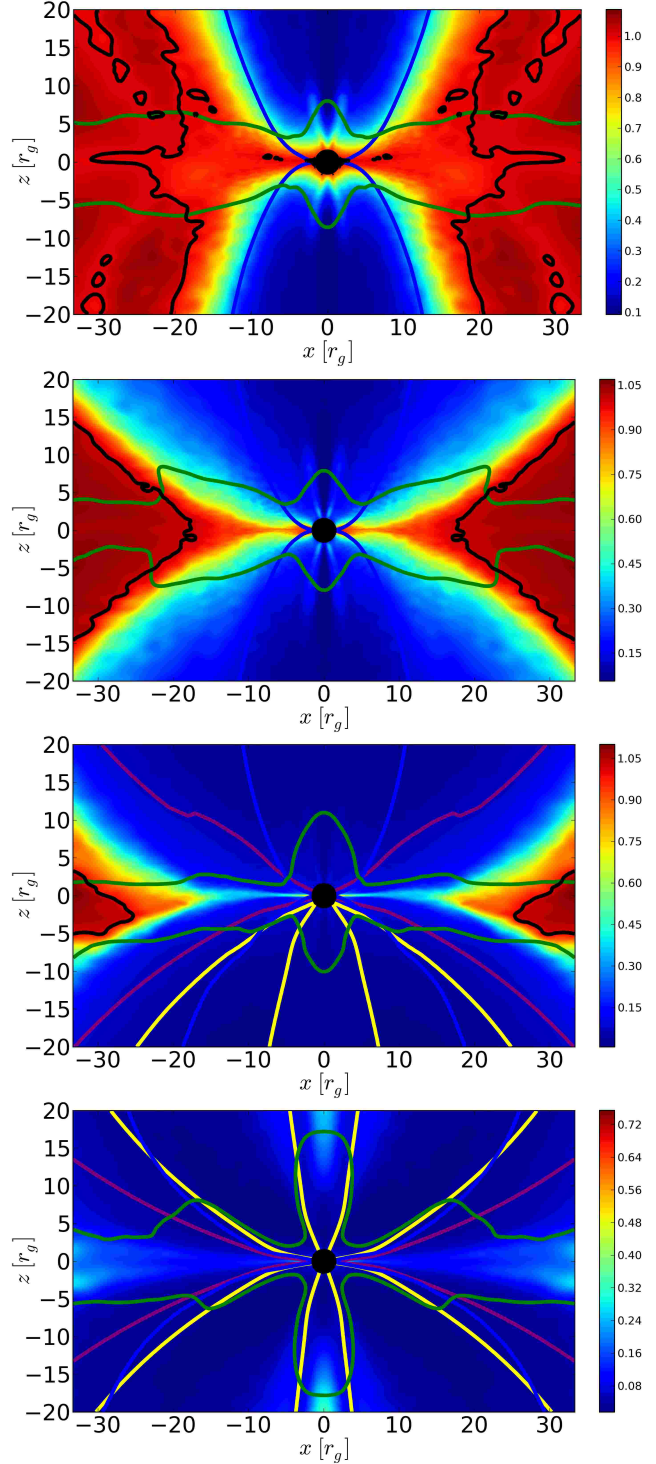


Figure 6. Model M1 at high $\dot{M} \sim 100\dot{M}_{\text{Edd}}$ (top panel), model M15 at lower $\dot{M} \sim 10\dot{M}_{\text{Edd}}$ (middle panel), model M14 at low $\dot{M} \sim 3\dot{M}_{\text{Edd}}$ (next panel), and model M13 at low $\dot{M} \sim 1\dot{M}_{\text{Edd}}$ (bottom panel), showing fluid-frame $\hat{T}_\gamma/T_{\text{gas}}$. Black line has $\hat{T}_\gamma/T_{\text{gas}} = 1$. Green, blue, yellow, and purple lines are, if present, as in Fig. 3. Models M13 and M14 have a photosphere near the disk, except the jet that is launched which keeps the density high to large radii. At high or low \dot{M} , the value of $\hat{T}_\gamma/T_{\text{gas}}$ is order unity due to thermal Comptonization. The disk is evidently thinner and cooler at lower mass accretion rates of $\dot{M} \sim 10\dot{M}_{\text{Edd}}$ even though the inflow is still quite super-Eddington. Only for the lowest $\dot{M} \sim \dot{M}_{\text{Edd}}$ model M13 does $\hat{T}_\gamma/T_{\text{gas}} \sim 0.1$ in the central disk, but progressively more coronal material has higher gas temperatures as \dot{M} drops.

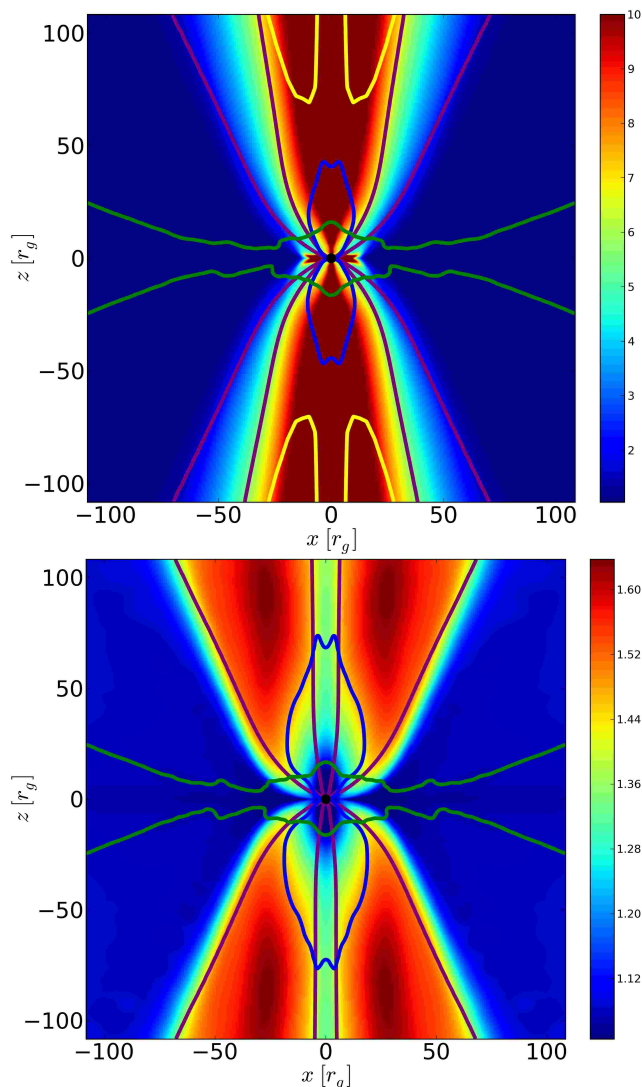


Figure 7. Models M7 and M8 with $a/M = 0$, which have no BH-spin-driven jet, showing lab-frame $f_{\text{col}} = T_{\gamma}/T_{\text{BB}}$ (numerator and denominator separately time- ϕ -averaged). Green, blue, yellow, and purple lines are, if present, as in Fig. 3. Without double Compton or synchrotron, the radiation beam has $f_{\text{col}} \sim 5$ (with overly high values in the funnel), while with these processes $f_{\text{col}} \sim 1.5$ – a significant reduction due to the high opacity of double Compton at high radiation temperatures and the plentiful soft photons produced by synchrotron in regions where $T_{\text{gas}} \gtrsim 10^8 \text{K}$.

itself regulates photon hardening away from large values seen in other simulations with no double Compton (e.g. M7).

Table 3 includes two models, M3 and M5, where M3 has a Bose-Einstein chemical potential, while M5 has a Planck chemical potential. The goal here is to see if chemical potential evolution has an effect in the case where neither double Compton or synchrotron are included. These models are dynamically quite similar as shown in Table 2. Table 3 shows significantly more photon hardening in the disk and radiation beam when using the Bose-Einstein chemical potential. This shows that the underlying assumption about the photon distribution has a strong effect on the photon hardening.

Fig. 8 shows how Wien the spectrum is, with the primary radiation beam in model M15 being down from Planck ($\exp(-\xi) = 1$) to $\exp(-\xi) \approx 0.85$. This distribution with radius and angle is typical for models with double Compton and synchrotron.

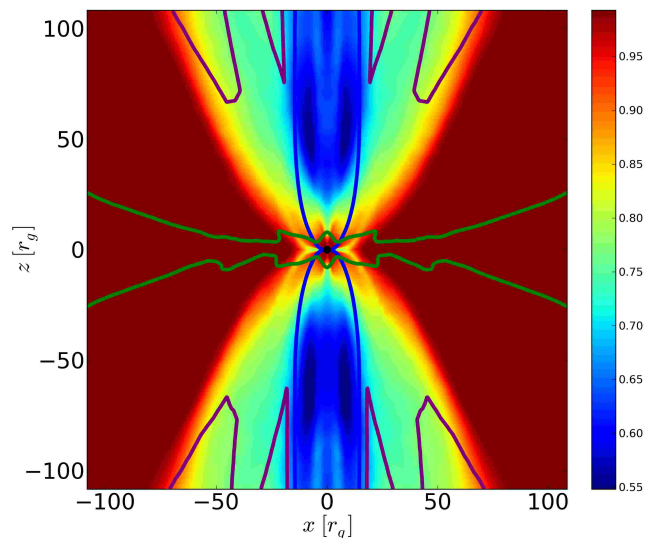


Figure 8. Model M15, showing fluid-Frame time- ϕ -averaged dimensionless chemical potential factor ($\exp(-\xi)$ given by Eq. A6, as color with legend) for the Bose-Einstein distribution. Green, blue, yellow, and purple lines are, if present, as in Fig. 3. The radiation beam is slightly Wien with $\exp(-\xi) \approx 0.85$, and the spatial distribution is similar for other models.

3.10 Radial and Angular Dependencies for All Models

Here we consider how radiative quantities are affected by photon conservation, opacity choices, etc. Quantities like rest-mass density, internal energy density, radiation-energy density, velocity, magnetic field, etc. behave like power-laws vs. radius within $r \sim 20r_g$ within the inflow equilibrium region. Such radial power-laws are typical of MADs (McKinney et al. 2012), so we do not discuss the radial behavior here.

Fig. 9 shows rest-mass density, gas temperature, and radiation to gas temperature ratio vs. θ . The gas temperatures are artificially high in models without thermal Comptonization or in models with photon number evolution that do not include double Compton and synchrotron. For example, models M2 and M10 do not include double Compton and synchrotron, while comparable models M1 and M9 do. Models with double Compton and synchrotron have much lower gas and radiation temperatures in the corona and jet. So, the thermodynamical and radiative properties of the disk, corona, and jet are only accurate with double Compton and synchrotron.

Fig. 10 shows the fluid-frame $\hat{T}_{\gamma}/T_{\text{gas}}$ (numerator and denominator separately time- ϕ -averaged) as weighted by rest-mass density times each grid cell volume size. This focuses the measurement of temperature on the core of the disk at the highest densities. Models at high \dot{M} have $\hat{T}_{\gamma} \sim T_{\text{gas}}$, and progressively lower \dot{M} down to $\dot{M} \sim \dot{M}_{\text{Edd}}$ have gas temperatures as high as ten times the radiation temperatures. Resolution should modify the results the most for the lowest \dot{M} models, but the model like M14 and M14h (at twice the ϕ resolution of M14) only show up to 30% relative differences. So, the corona region’s temperatures are roughly converged.

Fig. 10 also shows the fluid-frame \hat{T}_{γ} (weighted like $\hat{T}_{\gamma}/T_{\text{gas}}$ above). Lower $\dot{M} \sim \dot{M}_{\text{Edd}}$ are radiatively cooler than higher \dot{M} – even for super-Eddington rates. Compared to the temperatures in Sadowski & Narayan (2015a) that were for weakly-magnetized models at $\dot{M} \sim 10\dot{M}_{\text{Edd}}$, our results are comparable. However, our model M7 without double Compton and synchrotron demonstrates that our more magnetized disks would be much hotter if it were not for double Compton and synchrotron like included in model

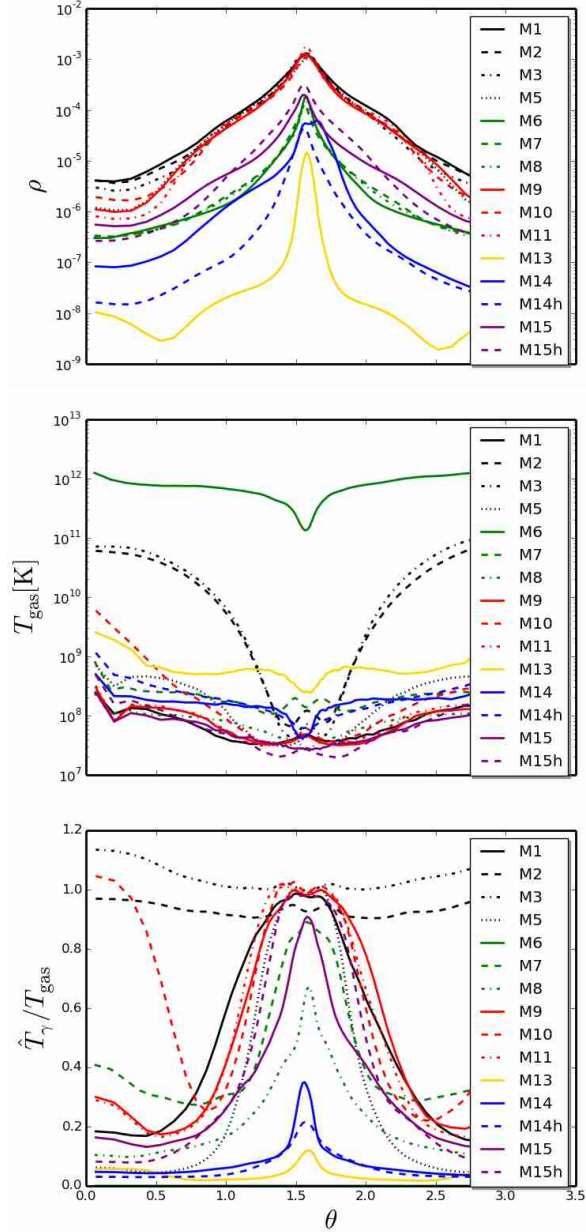


Figure 9. All models, showing fluid-frame density (ρ in g cm^{-3} , top panel), fluid-frame gas temperature (T_{gas} , second panel), and ratio of fluid-frame radiation to gas temperatures ($\hat{T}_\gamma/T_{\text{gas}}$, last panel) measured at $r = 10r_g$. Legend shows model types, where models are grouped by color for similar \dot{M} , a/M , or resolution changes for otherwise same initial density. M1-M5 are high $\dot{M} \sim 100\dot{M}_{\text{Edd}}$ models, M6-M8 are $a/M = 0$ models, M9-M11 are intermediate $\dot{M} \sim 50\dot{M}_{\text{Edd}}$ models, M13 is our lowest $\dot{M} \approx \dot{M}_{\text{Edd}}$ model, M14-M14h are our slightly higher $\dot{M} \approx 3\dot{M}_{\text{Edd}}$ models at different resolutions, and M15-M15h are intended to be $\dot{M} \approx 10\dot{M}_{\text{Edd}}$ models (but M15h ended up with much higher $\dot{M} \approx 30\dot{M}_{\text{Edd}}$). Lines are drawn in order from M1-M15h, so latter lines may overlap earlier lines. High \dot{M} models have a broader density profile compared to the more sharply-peaked low \dot{M} models. Models with high $\dot{M} \sim 100\dot{M}_{\text{Edd}}$ without double Compton and synchrotron (M2,M3) or models without thermal Comptonization (M6) have unphysically hot coronae and jets by three orders of magnitude in temperature, showing that these processes are crucial to include in order to obtain accurate thermodynamical and radiative properties in flows with $\dot{M} \gtrsim \dot{M}_{\text{Edd}}$.

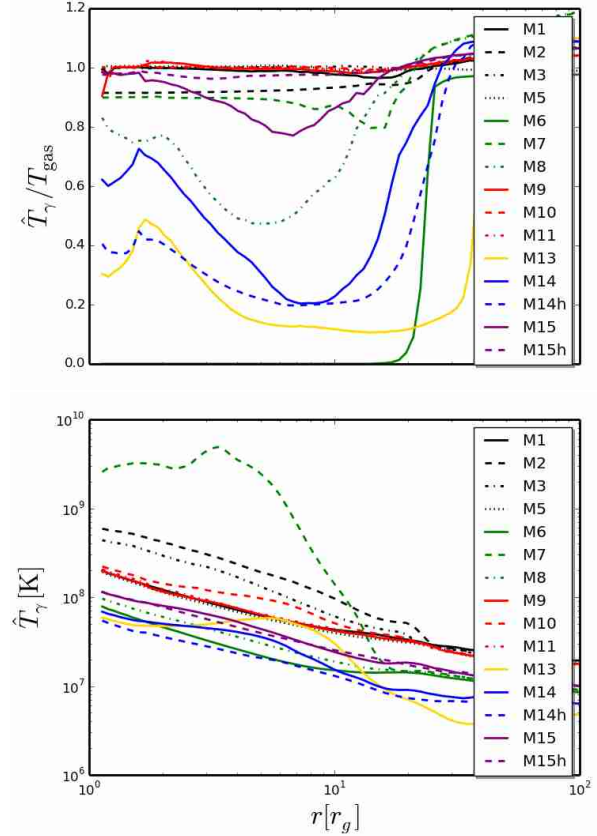


Figure 10. All models, showing fluid-frame $\hat{T}_\gamma/T_{\text{gas}}$ (top panel) and fluid-frame \hat{T}_γ (bottom panel) in the disk. Even for $\dot{M} \sim \dot{M}_{\text{Edd}}$, gas temperatures reach no more than ten times radiation temperatures at $r \sim 10r_g$ due to efficient thermal Comptonization. Higher \dot{M} tend to have higher radiation temperatures. Model M7 with photon number density evolution but without double Compton has much higher radiation temperatures than model M8 that has double Compton and is otherwise identical. Model M6 is like M7 but also has no thermal Comptonization, and as a consequence it has extremely high gas temperatures. These results demonstrate the importance of thermal Comptonization and double Compton as thermostats that, respectively, lower gas and radiation temperatures in the disk.

M8. So double Compton and synchrotron are required to regulate both gas and radiation temperatures in magnetized flows in general. Model M6 without thermal Comptonization shows extremely high gas temperatures, similar to seen in Takahashi et al. (2016), but thermal Comptonization severely limits the difference between gas and radiation temperatures by driving them toward equilibrium.

Fig. 11 shows the fluid-frame $\hat{f}_{\text{col}} = \hat{T}_\gamma/T_{\text{BB}}$, weighted like $\hat{T}_\gamma/T_{\text{gas}}$ above. The photon distribution within the disk is essentially Planckian at large radii but for low $\dot{M} \sim \dot{M}_{\text{Edd}}$ the distribution becomes harder at intermediate radii of $r \sim 5r_g$. Model M7 (without double Compton and synchrotron, as compared to otherwise identical model M8 with double Compton and synchrotron) has excessive unphysical hardening even in the disk due to photon conserving Comptonization driving the photon distribution toward Wien.

Fig. 11 also shows the fluid-frame chemical potential factor $\exp(-\xi)$ given by Eq. (A6), weighted like $\hat{T}_\gamma/T_{\text{gas}}$ above. The photon distribution within the disk is essentially Planckian at large radii, but for low $\dot{M} \sim \dot{M}_{\text{Edd}}$ (e.g. model M13) the distribution becomes more Wien as densities become small enough that there is inefficient photon production.

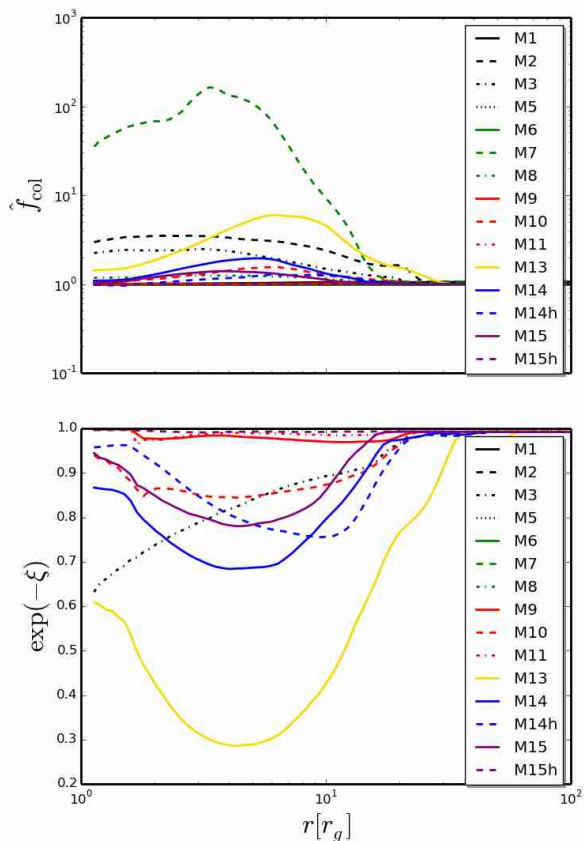


Figure 11. All models, showing fluid-frame \hat{f}_{col} (top panel) and chemical potential factor $\exp(-\xi)$ (bottom panel) in the disk. Lower \dot{M} (e.g. M13) tend to have regions in the disk around $r \sim 5r_g$ where the disk photon distribution is hardened, while at high \dot{M} the disk photons are essentially Planckian as long as double Compton and synchrotron are included. Model M2, M3, and M7 have no double Compton or synchrotron, leading to unphysically large photon hardening in the disk. This shows that double Compton and synchrotron are required in order to accurately track photon hardening.

Fig. 12 shows the ratio of double Compton to free-free opacities (units cm^{-1} , which includes a density scale) with no additional weighting, as averaged over a density scale height for each simulation at each radius. Higher \dot{M} lead to progressively more importance of double Compton relative to free-free within the equatorial disk region. For $\dot{M} \sim 10\dot{M}_{\text{Edd}}$, double Compton dominates free-free within $r \sim 8r_g$, within which significant radiation is generated.

Table 3 includes models M1 and M2 that primarily differ in that M1 includes double Compton and synchrotron while M2 does not. Double Compton and synchrotron provide plentiful soft photons that lead to much lower photon hardening than seen in M2, so this shows that double Compton and synchrotron are crucial to include in highly-magnetized MAD-type super-Eddington flows with $\dot{M} \sim 100\dot{M}_{\text{Edd}}$.

Fig. 13 shows the synchrotron opacity divided by the free-free opacity in the disk as well as b^2/ρ (each b^2 and ρ weighted with density like done for $\hat{T}_\gamma/T_{\text{gas}}$ above) in the disk. At small radii, where magnetic energy density approaches rest-mass energy density, synchrotron dominates free-free in the disk for rapidly rotating black hole models. This is due to the jet and its interaction with the disk in a MAD state, where at $r = 10r_g$, the orthonormal B^θ is ten times higher at $a/M = 0.8$ than at $a/M = 0$ outside the disk.

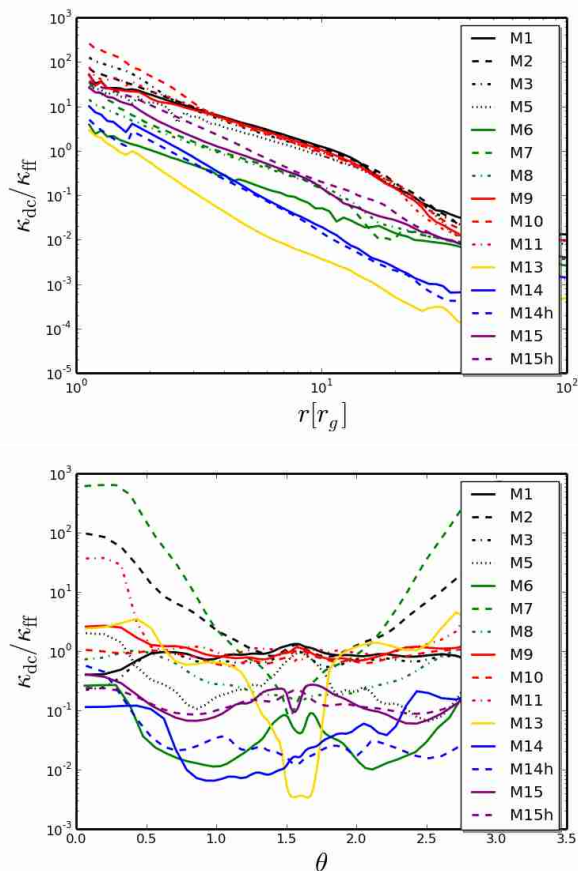


Figure 12. All models, showing fluid-frame double Compton opacity divided by free-free opacity in the disk (top panel) and across the disk at $r = 10r_g$ (bottom panel). Some models, like M2, M3, M5, M7, and M10, have no double Compton and show excessive double Compton opacity because it was not present to regulate the radiation temperature to lower values. For $\dot{M} \sim \dot{M}_{\text{Edd}}$ double Compton dominates free-free inside the disk within $r < 3r_g$, for $\dot{M} \sim 10\dot{M}_{\text{Edd}}$ double Compton dominates free-free inside the disk within $r < 8r_g$, and for $\dot{M} \sim 100\dot{M}_{\text{Edd}}$ double Compton dominates free-free inside the disk within $r < 15r_g$ (and potentially further if simulation duration was extended, as inflow equilibrium is only out to $r \sim 20r_g$). Comparing non-rotating black hole models M7 (no double Compton) and M8 (with double Compton), double Compton acts as a thermostat that keeps the plasma in a state where free-free and double Compton are comparable in the corona. Since significant radiation emerges from within $r = 10r_g$ and the temperature of the corona affects the radiation that reaches large radii, double Compton is an important process to include for highly-magnetized super-Eddington accretion flows.

Fig. 14 shows the synchrotron energy opacity to free-free energy opacity across the disk as well as b^2/ρ (with ρ evaluated at the equator) across the disk at $r = 10r_g$. Synchrotron is not important as an energy opacity in the disk at such radii, but in the jet is the dominant process due to the large magnetic energy density.

By contrast, the synchrotron number opacities in the disk, corona, and jet dominate the free-free (and even OPAL) opacities out to $r \sim 20r_g$ for $\dot{M} \gtrsim 100\dot{M}_{\text{Edd}}$, out to $r \sim 5r_g$ for $\dot{M} \gtrsim 3\dot{M}_{\text{Edd}}$, and only in the jet for nearly sub-Eddington accretion rates. This is due to the relatively large $\phi \gtrsim 10^3$ (Eq. D5) while also having relatively stronger magnetic fields at higher accretion rates.

Model M6 without thermal Comptonization shows an artificial

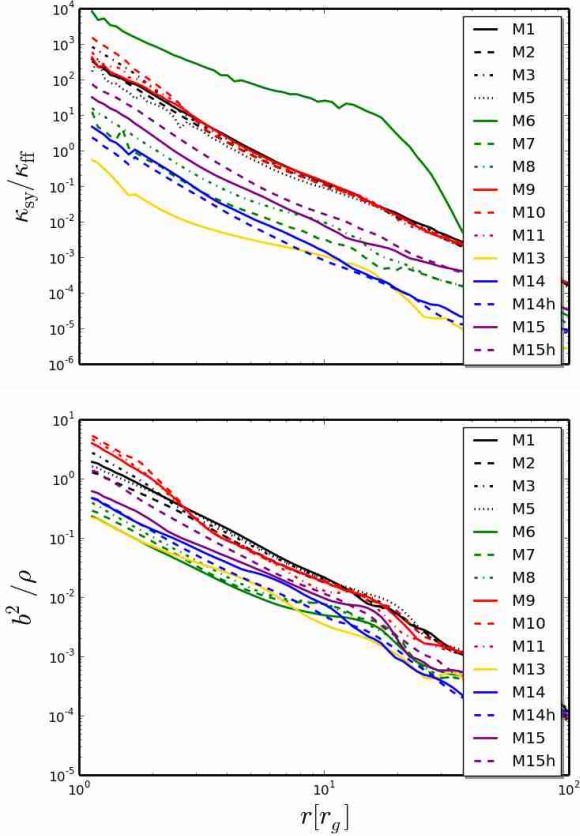


Figure 13. All models, showing fluid-frame synchrotron opacity divided by free-free opacity in the disk (top panel) and b^2/ρ in the disk (bottom panel). Synchrotron dominates free-free in the disk at small radii once temperatures rise to $T \sim 10^8\text{K}$ and $b^2/\rho \sim 1$. Low $\dot{M} \sim \dot{M}_{\text{Edd}}$ models only have comparable synchrotron and free-free quite close to the horizon, but higher \dot{M} have progressively important synchrotron that dominates free-free to larger radii – out to $r \sim 5r_g$ for $\dot{M} \sim 100\dot{M}_{\text{Edd}}$. Model M6 has no thermal Comptonization or synchrotron, so gas temperatures and synchrotron emission opacities are unphysically high. For models with thermal Comptonization, synchrotron is not important in the central disk except for quite high \dot{M} .

dominance of synchrotron due to the artificially high gas temperatures, which are suppressed by thermal Comptonization.

4 SUMMARY

We have incorporated several new opacity effects within HARM-RAD as applicable to black hole accretion flows accreting at Eddington to super-Eddington rates. We investigated a range of accretion rates from $\dot{M} \sim 1\dot{M}_{\text{Edd}}$ up to $\dot{M} \sim 100\dot{M}_{\text{Edd}}$ in order to consider how thermal Comptonization, double Compton, synchrotron, and other opacity effects control the thermodynamic and radiative properties of highly-magnetized MAD type accretion flows.

We found that double Compton dominates free-free in the central core of the disk even out to fairly large radii of $r \sim 15r_g$ (and potentially much further if we considered longer duration simulations) in highly super-Eddington accretion flows with $\dot{M} \sim 100\dot{M}_{\text{Edd}}$. We also found for these MAD models that synchrotron dominates free-free within $r \sim 5r_g$ for highly super-Eddington accretion flows, and synchrotron provides plentiful soft photons to regulate radiation temperatures throughout the flow for

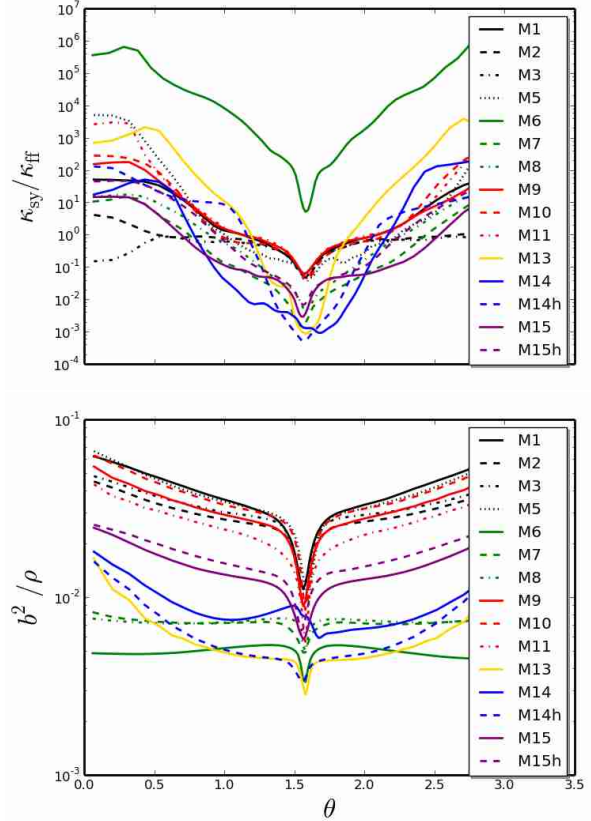


Figure 14. All models, showing fluid-frame synchrotron opacity divided by free-free opacity as well as b^2/ρ (using density at equator for b^2/ρ) across the disk at $r = 10r_g$. Synchrotron becomes as important as free-free in the corona in models with $\dot{M} \sim 100\dot{M}_{\text{Edd}}$ and becomes much more important than free-free in the jet for most models. So synchrotron is crucial to include for the corona and jet thermodynamics in highly-magnetized MAD models with $\dot{M} \gtrsim \dot{M}_{\text{Edd}}$.

$\dot{M} \gtrsim 10\dot{M}_{\text{Edd}}$. Progressively lower accretion rates are dominated by double Compton and synchrotron within progressively smaller radii until for sub-Eddington accretion these processes do not dominate in the central core of the disk.

For our MAD models, we found that the coronal gas and radiation temperatures are regulated by double Compton and synchrotron, while jet temperatures are regulated by synchrotron. Of our more realistic models with all our opacity physics, our model with $\dot{M} \approx \dot{M}_{\text{Edd}}$ shows the highest disk gas temperatures compared to higher accretion rate models. The surrounding coronal gas has temperatures of $T_e \approx 7 \times 10^8\text{K}$ corresponding to 60keV, which is ≈ 100 times higher than the disk’s black body temperature and ≈ 20 times higher than the disk’s radiation temperature (hardened by $f_{\text{col}} \approx 4.5$). This compares to other recent local shearing box simulations that studied coroneae and saw only up to $T \sim 10^7\text{K}$ in the corona and a factor of 10 cooler disk black body temperatures (Jiang et al. 2014b). The polar jet region near the black hole has $T_e \sim 4 \times 10^9\text{K}$ corresponding to 350keV, about ten times higher than models with $\dot{M} \approx 30\dot{M}_{\text{Edd}}$, which should also contribute to Comptonized emission (O’ Riordan et al. 2016b,a). The gas heating in the corona is plausibly driven by the strong highly-dynamic magnetic fields threading the black hole and MAD type disk, but more detailed analysis of this state will be presented in future work.

Thermal Comptonization with double Compton and synchrotron were crucial to include, otherwise gas temperatures were excessively high by factors of ten (with thermal Comptonization, but without double Compton or synchrotron) and up to factors of a thousand (when no thermal Comptonization is included) as seen in Takahashi et al. (2016). However, their suggestion that hot gas regions could lead to the very high state (Kubota & Done 2004) might still apply to our model with $\dot{M} \sim \dot{M}_{\text{Edd}}$, which has disk gas temperatures ten times higher than disk radiation temperatures.

We also found that for rotating black hole models, the isotropic equivalent luminosity is enhanced compared to the total luminosity by a beaming factor of up to $b = 12$ for the jet and up to $b = 8$ for the radiation. Non-rotating models show only moderate beaming of the jet by $b = 5$ and radiation by factor $b \sim 2-3$, which agrees with Sądowski & Narayan (2015b). The rotating black hole models with significant beaming of radiation could help explain ultra-luminous X-ray sources (ULXs).

None of our models show signs of thermal instability, as consistent with our prior studies of super-Eddington flows (McKinney et al. 2014, 2015). The stability of radiation-dominated disks is uncertain, but affected by numerical method details, opacities used, the degree of magnetization, and how these lead to enhanced advection (Hirose et al. 2009; Jiang et al. 2013; Sądowski 2016; Jiang et al. 2016; Mishra et al. 2016). Free-free does not limit the thermal instability for increasing temperatures due to its opacity dropping, but processes like double Compton increase with temperature and so might ultimately limit such runaways.

The primary limitation of our study is the use of the M1 closure approximation because rays cannot intersect in the optically thin regime. This limits applications to cases where most of the radiation is in the scattering-dominated regime (true for all of our models in the disk, and true for many of our models out to large radii) or where radiation emerges primarily from a single region (as common in accretion disks, for which radiation comes from near the BH) (Tsang & Milosavljević 2015). Multi-frequency transport could also be important (Roberts et al. 2016).

Our study is most relevant to observations related to tidal disruption events (TDEs) (Dai et al. 2015), super-Eddington black hole X-ray binary systems like GRS1915+105 and SS433 (Kulkarni et al. 2011), ULXs, and numerous quasars that accrete near or above Eddington. Our results show that radiation beaming and photon hardening effects are strong, and that Eddington to super-Eddington models require double Compton and synchrotron in order to obtain accurate temperatures in the corona and jet. Double Compton may be an important thermostat (that enforces slightly lower temperatures than pair creation seen in Fabian et al. 2015) in quasars and other radiatively efficient super-massive BHs. Either improvements to our radiative transfer scheme or multi-frequency radiative transfer post-processing (Narayan et al. 2016) could allow these simulations to be compared directly with spectra and timing from these systems (Castelló-Mor et al. 2016).

ACKNOWLEDGMENTS

JCM thanks Jane Dai for useful discussions and acknowledges support by NASA/NSF/TCAN (NNX14AB46G) as well as computing time from NSF/XSEDE/TACC (TG-PHY120005) and NASA/Pleiades (SMD-14-5451). JC acknowledges support by the Royal Society as a Royal Society University Research Fellow at the University of Manchester, UK. MW acknowledges support of the Foundation for Polish Science within the START programme

and the Polish NCN grant UMO-2013/08/A/ST9/00795 RN was supported in part by NSF grant AST1312651 and NASA grant NNX14AB16G. AS acknowledges support by NASA through the Einstein Postdoctoral Fellowship number PF4-150126.

APPENDIX A: BOSE-EINSTEIN PHOTON DISTRIBUTION

The fluid-frame quantities E and n described in §2 provide two parameters that describe the photon distribution function. All quantities in these appendices are in the fluid frame. A reasonable assumption for general optical depths is a Bose-Einstein (BE) distribution (Miller et al. 2011), which correctly captures the behavior of the photon distribution in a scattering-dominated atmosphere and how it goes from Planck to Wien as radiation and gas temperatures equilibrate. A diluted Planck might be reasonable in some cases (Sądowski et al. 2016). We assume BE holds in the fluid frame, which will be valid in the optically thick regime or when the radiation is fairly isotropic in the fluid frame and energy exchange with the electrons drives the photon distribution towards kinetic equilibrium. This neglects Doppler effects, because the radiation should be isotropic in its own frame according to the M1 closure.

Let us define $x = hv/(k_b T_\gamma)$ and $\xi = \mu/(k_b T_\gamma)$. Then the Bose-Einstein distribution function is

$$n_x = \frac{e^{-\xi}}{e^x - e^{-\xi}}. \quad (\text{A1})$$

The angle-integrated distribution of photons is given by the number distribution

$$BNdx = C(k_b T_\gamma)^3 e^{-\xi} \frac{x^2 dx}{e^x - e^{-\xi}} = C(k_b T_\gamma)^3 e^{-\xi} dI_n, \quad (\text{A2})$$

with $C = (8\pi)/(h^3 c^3)$. The corresponding energy distribution is

$$BEDx = C(k_b T_\gamma)^4 e^{-\xi} \frac{x^3 dx}{e^x - e^{-\xi}} = C(k_b T_\gamma)^4 e^{-\xi} dI_E. \quad (\text{A3})$$

Then, the radiation number and energy densities are

$$n(\xi) = C(k_b T_\gamma)^3 e^{-\xi} I_n(\xi), \quad (\text{A4a})$$

$$E(\xi) = C(k_b T_\gamma)^4 e^{-\xi} I_E(\xi), \quad (\text{A4b})$$

respectively. This corresponds to two equations and two unknowns for T_γ and ξ (or equivalently $e^{-\xi}$).

Solving these equations, one obtains $e^{-\xi} = n^4 I_E^3 / (C E I_n^4)$ and $k_b T_\gamma = E I_n / (I_E n)$. Noting the behavior of T_γ and $e^{-\xi}$ is like exponentials, and searching for a simple fitting function to avoid an inversion of a Polylog, we find a fit for radiation temperature of

$$k_b T_\gamma = \frac{E/n}{0.33333 + 0.060725/(0.646756 + 0.121982CE^3/n^4)} \quad (\text{A5})$$

with a corresponding equation for the chemical potential (μ) written in terms of a dimensionless $\xi = \mu/(k_b T_\gamma)$ as

$$e^{-\xi} = \frac{1.64676}{0.646756 + 0.121982CE^3/n^4}. \quad (\text{A6})$$

These fits agree with the full solution to $< 2\%$ from Planck ($\mu = 0$) to Wien ($\mu \rightarrow \infty$) limits. To match the Bose-Einstein condensate limit $\mu = 0$ when $T_\gamma \rightarrow 0$, we restrict $e^{-\xi} < 1$, while T_γ naturally tends to zero as $n \rightarrow \infty$ for fixed E . Now given the equations of motion value for E and n , we can obtain T_γ and $e^{-\xi}$ that are used to compute any opacity or emission rate.

Note that for Planck distributions, the integration over the BE_ν

distribution function gives $u_0 = B(4\pi/c)$ with Planck photon energy density of $u_0 = aT^4$ (a is the radiation constant) and integration over the BN_γ distribution gives $n_0 = (30\text{Zeta}(3)/\pi^4)(a/k_b)T^3 \approx (1/2.7)(u_0/(k_bT))$ where $N = n_0c/(4\pi)$.

More generally, a BE distribution can be considered as a rough fit to the frequency position of the peak and the shape of the soft photon portion for the general distribution n_x . This fit would break-down when the emission is optically thin and absorption occurs far from the peak in emission.

APPENDIX B: MEAN EMISSION AND ABSORPTION

Here we discuss how the mean opacity should be computed for Boltzmann moment methods like the M1 closure method. Here, the emitted mean intensity is $j_\nu = e_\nu/(4\pi)$ and e_ν is the emissivity (energy loss per unit volume per unit time per unit frequency). The energy loss rate per unit volume is then $\lambda_e = \int e_\nu d\nu$.

B1 Integrated evolution equations

We obtain the form of Kirchhoff's law and the correct mean opacity from the Boltzmann equation in the fluid frame in a homogeneous plasma without Compton scattering (not required to obtain our result). The Boltzmann equation for the photon occupation number n_x with $x \equiv h\nu/(k_bT_\gamma)$ and $x_e \equiv h\nu/(k_bT_e)$, caused by bremsstrahlung (BR) and double Compton (DC) emission without Kompaneets, reads

$$\begin{aligned} \partial_\tau n_x &= \frac{\Lambda_{\text{BR}}(x, T_\gamma, T_e)}{x^3} [1 - n_x(e^{x_e} - 1)] \\ &+ \frac{\Lambda_{\text{DC}}(x, T_\gamma, T_e)}{x^3} [1 - n_x(e^x - 1)], \end{aligned} \quad (\text{B1})$$

in the fluid-frame for a fluid element with proper time τ , where $\Lambda_X(x, T_\gamma, T_e)/x^3 = dn_x/dt$ of emission, describes the respective emission rates (excluding stimulated emission). The BR process drives the photon occupation number towards a black-body at temperature T_e , i.e., $n_x = 1/(e^{x_e} - 1)$, while DC pushes towards a black-body at temperature T_γ , i.e., $n_x = 1/(e^x - 1)$ (see §E3). Neither of these two solutions make the Boltzmann collision term vanish for $T_e \neq T_\gamma$ and the general equilibrium solution with respect to the BR and DC processes is given by

$$n_x^{\text{eq}} = \left(\frac{\Lambda_{\text{BR}}e^{x_e} + \Lambda_{\text{DC}}e^x}{\Lambda_{\text{BR}} + \Lambda_{\text{DC}}} - 1 \right)^{-1}. \quad (\text{B2})$$

As expected, for $T_e = T_\gamma$ this reduces to $n_x^{\text{eq}} = 1/(e^x - 1)$. So assuming a BE-type distribution is only accurate in the equilibrium limit when a single process dominates at some point in time and space or if $T_\gamma \sim T_e$, the latter being true in equilibrium because we include thermal Comptonization.

From Eq. (B1), we wish to obtain evolution equations for the moments $N_\gamma = \int x^2 n_x dx$ and $\rho_\gamma = \int x^3 n_x dx$ of the photon distribution. We furthermore want to express the equations in a form $\partial_\tau N_\gamma = \Lambda_N - \kappa_N N_\gamma$ and $\partial_\tau \rho_\gamma = \Lambda_\rho - \kappa_\rho \rho_\gamma$, where the coefficients Λ_i and κ_i are functions of the two temperatures and possible dependent parameters describing the underlying photon distributions function. To obtain integrated equations one has to make an ansatz for n_x , which is given by only two *free* parameters, since only two moments of the Boltzmann equation are being used (N_γ and ρ_γ).

Let us start with N_γ . Inserting $n_x = n_{\text{BE}} = 1/(e^{x+\mu} - 1)$ into Eq. (B1) with a cutoff x_c yields

$$\begin{aligned} \partial_\tau N_\gamma(T_\gamma, \mu) &= \int_{x_c}^{\infty} \frac{\Lambda_{\text{BR+DC}}(x, T_\gamma, T_e)}{x} dx \\ &- \int_{x_c}^{\infty} \frac{\Lambda_{\text{BR}}(x, T_\gamma, T_e)}{x} \frac{e^{x_e} - 1}{e^{x+\mu} - 1} dx \\ &- \int_{x_c}^{\infty} \frac{\Lambda_{\text{DC}}(x, T_\gamma, T_e)}{x} \frac{e^x - 1}{e^{x+\mu} - 1} dx, \end{aligned} \quad (\text{B3})$$

so that one has the emission and absorption coefficients

$$\Lambda_N = \int_{x_c}^{\infty} \frac{\Lambda_{\text{BR+DC}}}{x} dx \quad (\text{B4a})$$

$$\kappa_N = \frac{1}{N_\gamma(T_\gamma, \mu)} \left[\int_{x_c}^{\infty} \frac{\Lambda_{\text{BR}}(e^{x_e} - 1) + \Lambda_{\text{DC}}(e^x - 1)}{x(e^{x+\mu} - 1)} dx \right] \quad (\text{B4b})$$

Similarly, for ρ_γ we find

$$\Lambda_\rho = \int_{x_c}^{\infty} \Lambda_{\text{BR+DC}} dx \quad (\text{B5a})$$

$$\kappa_\rho = \frac{1}{\rho_\gamma(T_\gamma, \mu)} \left[\int_{x_c}^{\infty} \frac{\Lambda_{\text{BR}}(e^{x_e} - 1) + \Lambda_{\text{DC}}(e^x - 1)}{e^{x+\mu} - 1} dx \right]. \quad (\text{B5b})$$

One can also obtain the moment equation associated with momentum conservation, which would introduce a radiation flux (and so radiation frame velocity in the M1 closure) as a weight. We do not try to model the angular distribution and frequency dependence on the M1 radiation velocity, and in general the M1 flux mean behaves in a more complicated way as a function of optical depth (Struchtrup 1997; Christen & Kassubek 2014).

These equations shows how one must construct α_ν via the correct Kirchhoff's law (i.e. which temperature enters) and the related mean opacity (i.e. how to weight the emission rate), where $\lambda = C(k_b T_\gamma)^4 \Lambda_\rho$, $\lambda_n = C(k_b T_\gamma)^3 \Lambda_N$, $\kappa_a = \kappa_\rho/c$, and $\kappa_{an} = \kappa_N/c$.

B2 Kirchhoff's Law

The opacity for each process, α_ν (in cm^{-1} , where κ , in the same units, is reserved for the mean opacity), for a thermal electron distribution is given by Kirchhoff's law

$$\alpha_\nu = \frac{j_\nu}{B_\nu(T_{\text{eq}}, \mu_{\text{eq}})}, \quad (\text{B6})$$

where the last section shows that $T_{\text{eq}} = T_e$ for a process like BR and $T_{\text{eq}} = T_\gamma$ for a process like DC, where $\mu_{\text{eq}} = 0$.

B3 Mean Opacities

We use an approximation to the absorption mean, flux mean, and emission mean that enter the 4-force. For a more general discussion, see section 82 of Mihalas & Mihalas (1984), section 2.3 of Huebner & Barfield (2014), page 38 in Sturrock et al. (1986), page 174 in Castor (2004), or section 15.2 in Modest (2013).

The Planck or emission mean is

$$\kappa_p = \frac{\int_\nu \alpha_\nu B_\nu}{\int_\nu B_\nu} = \frac{\int_\nu j_\nu}{\int_\nu B_\nu} = j/B = e/(4\pi B), \quad (\text{B7})$$

for optically thin emission rate e . The Planck mean would be what is required if the radiation were LTE and one wanted to ensure the

optically thin emission rate was correct if using our 4-force in the comoving frame with an energy loss rate of

$$du_g/d\tau = \kappa_a(E - 4\pi B), \quad (\text{B8})$$

such that in the limit that $E \rightarrow 0$ as $\tau = \kappa_a L \rightarrow 0$ for some length L of the region, then the gas would lose energy at a rate of $4\pi\kappa_a B = e \equiv \lambda_e$ as required.

In the LTE diffusion limit, the Rosseland mean opacity κ_R with

$$\kappa_R^{-1} = \frac{\int_v \alpha_v^{-1} dB_v/dT}{\int_v dB_v/dT} \quad (\text{B9})$$

is a good approximation to the flux mean (Davis et al. 2014). The Rosseland mean should not be generally used in the energy equation as it would fail to give the correct emission rate in the optically thin limit. Another approach is the use the Planck or absorption mean for the energy equation while using the Rosseland mean to approximate the flux mean for the momentum equation (Sadowski et al. 2016), but this only gives a correct momentum exchange in the diffusive limit for each grid cell.

Section B1 shows that the opacity which enters the energy and number equations is the absorption mean given by

$$\kappa_A = \frac{\int_v \alpha_v J_v}{\int_v J_v} \quad (\text{B10})$$

for a mean intensity $J_v = \int_{4\pi} I_v d\Omega/(4\pi)$ of radiation. Nominally, one might not know or it may be hard to model J_v , but we model the distribution function as BE. The absorption mean has also been called the two-temperature Planck mean, and it has been used to handle irradiated planetary atmospheres (Hubeny et al. 2003; Heng et al. 2012) and circumstellar atmospheres (Malygin et al. 2014).

For the momentum equation and its flux mean, the mean absorption opacity should vary from the full Rosseland mean (including every emission process and scattering in a single integration) in the diffusion limit to the above absorption mean in the streaming limit. This could be approximately achieved by interpolation (Sampson 1965; Patch 1967; Ludwig et al. 1994; Vögler et al. 2004), or by splitting the trapped and streaming radiation (e.g., Rosdahl & Teyssier 2015) with different opacities for each component. For simplicity, we use the same way of computing the absorption mean opacity for the energy, number, and momentum equations. This may be reasonable for accretion disks, whose global photospheres are often optically thin across each grid cell where source terms are applied. In the deep optically thick limit within the disk, the diffusion times are often slower than an inflow or outflow time. Then, radiation is trapped in the flow, so that the opacity just needs to be high enough to maintain trapping.

The energy absorption energy-mean opacity is given by

$$\kappa_a = \frac{\int_v \alpha_v BE_v(T_{\text{abs}}, \mu_{\text{abs}})}{\int_v BE_v(T_{\text{abs}}, \mu_{\text{abs}})}. \quad (\text{B11})$$

for a Bose-Einstein energy distribution BE . The corresponding number absorption number-mean opacity is given by

$$\kappa_{an} = \frac{\int_v \alpha_v BN_v(T_{\text{abs}}, \mu_{\text{abs}})}{\int_v BN_v(T_{\text{abs}}, \mu_{\text{abs}})}. \quad (\text{B12})$$

for a Bose-Einstein number distribution BN . For the distribution BE and BN , one must choose $T_{\text{abs}} \rightarrow T_\gamma$ and $\mu_{\text{abs}} \rightarrow \mu$ for an ambient BE radiation field at temperature T_γ and chemical potential μ as consistent with Eq. (B1). The lower integration range over frequency is assumed to be set by the Razin effect for each process.

Note that if one used κ_a instead of κ_{an} in the number evolution equation, it would not give back a consistent optically thick thermal equilibrium density of photons. From Eq. (9), one would have obtained $c\kappa_a n = \lambda_n$. However, the denominator of κ_a integrates to $B = u_0 c/(4\pi)$ while the numerator of κ_a integrates to the energy density loss rate per solid angle $\lambda_e/(4\pi)$. So one would have obtained an equilibrium number density of $n = \lambda_n/(c\kappa_a) = u_0 \lambda_n/\lambda_e$, which while dimensionally correct is not the required Planck answer of n_0 . However, by using the number absorption number-mean opacity, one obtains an equilibrium number density from $c\kappa_{an} n = \lambda_n$ giving $n = \lambda_n/(c\kappa_{an}) = n_0$ as required.

B4 Modifying the BE distribution with inverse Compton and self-absorption

An ambient photon distribution as BE with a frequency independent $\mu_{\text{abs}} \neq 0$ is only a reasonable assumption if the absorption timescale is longer than a typical flow timescale t_{flow} and longer than the timescale for inverse Comptonization to upscatter photons (and so avoid absorption). Otherwise, if absorption is effective, then $\mu_{\text{abs}} \rightarrow 0$ (Sunyaev & Zeldovich 1970; Lightman 1981; Burigana et al. 1991, 1995). Because DC and bremsstrahlung emission become increasingly effective at low frequencies, this condition is always fulfilled at very low frequencies.

When $k_b T_e \lesssim m_e c^2$, the timescale for inverse Comptonization (IC) of photons to higher energies is

$$t_{\text{IC}} \sim t_e \frac{m_e c^2}{k_b T_e} \quad (\text{B13})$$

where $t_e = (n_e c \sigma_T)^{-1}$ is the electron scattering timescale. (This is not the energy redistribution time between gas the electrons, that would given by $t_{\text{re}} \sim E/\lambda_e$ from Eq. (E2).) The timescale for absorption is given by the absorption term for dn_x/dt in Boltzmann's equation and computing

$$t_{\text{abs}} \sim \frac{n_x}{[dn_x/dt]_{\text{abs}}} = \frac{1}{c\alpha_x}, \quad (\text{B14})$$

where $\alpha_x = \alpha_v$. From the condition $t_{\text{IC}} \geq t_{\text{abs}}$, one can thus determine those frequencies for which the distribution is Planck because those low-energy photons are absorbed before being upscattered.

So, a significant improvement to the BE distribution assumption is to force $\mu_{\text{abs}} \rightarrow 0$ when $t_{\text{abs}} < t_{\text{flow}}$ and $t_{\text{abs}} < t_{\text{IC}}$ for a typical flow time or simulation timestep $t_{\text{flow}} \sim 10^{-3}(r_g/c)$. Otherwise, IC avoids self-absorption or insufficient time has elapsed to assume absorption has had time to force $\mu_{\text{abs}} \rightarrow 0$. This is how we modify the BE distribution in this paper. We do not try to model the transition and just assume it's a discontinuous change in the distribution. This modified BE distribution acts as a sub-timestep model for the photon distribution function. We apply this modification to μ for each process, which assumes the dominant process is the only one we need to treat accurately.

B5 Absorption balancing Emission

The energy emission rate is

$$\lambda_e = 4\pi \int_v j_v = 4\pi \int_v \alpha_v BE_v = \kappa_a 4\pi \int_v BE_v \equiv \kappa_e 4\pi B, \quad (\text{B15})$$

with the last equation defining the so-called energy emission mean opacity κ_e . The number emission rate is

$$\lambda_n = 4\pi \int_v (j_v/(h\nu)) = 4\pi \int_v \alpha_v BN_v = \kappa_{an} 4\pi \int_v BN_v \equiv \kappa_{en} 4\pi N, \quad (\text{B16})$$

where κ_a and κ_{an} are from the generalized absorption mean opacity expression Eq. (B11) and Eq. (B12). For these emission processes, in the distribution functions *BE* and *BN* that appear in κ_a and κ_{an} , one replaces $T_{\text{abs}} \rightarrow T_{\text{eq}}$ ($T_{\text{eq}} = T_e$ for BR-like processes and $T_{\text{eq}} = T_\gamma$ for DC-like processes) and $\mu_{\text{abs}} \rightarrow \mu_{\text{eq}} = 0$.

This construction of λ_e and λ_n just ensures that we treat the integration limits consistently so that in the optically thick thermal equilibrium limit the absorption balances emission. It also defines the so-called emission mean opacity that is just a way to write the emission rates as a type of opacity with a simple factor *B* or *N* that need not be separately tabulated.

APPENDIX C: FREE-FREE EMISSION

Following the discussion in Rybicki & Lightman (1986) that follows Novikov & Thorne (1973), the electron-ion free-free emissivity J_ν^{ffei} is obtained from

$$J_\nu^{\text{ffei}} = \frac{8 \sqrt{\frac{2\pi}{3}} (n_- + n_+) n_i q^6 Z_p^2 \sqrt{\frac{1}{k_b m_e}} e^{-\frac{h\nu}{k_b T_e}}}{3c^3 m_e \sqrt{T_e}} \bar{g}_{\text{ffei}} R_{\text{ei}}(\theta), \quad (\text{C1})$$

where we assume no pairs so $(n_- + n_+) \rightarrow n_e$, and where the relativistic correction factor is

$$R_{\text{ei}}(\theta_e) = \begin{cases} 1 + 1.76\theta_e^{1.34} & \theta_e \leq 1 \\ 1.4\theta_e^{0.5} (\ln(1.12\theta_e + 0.48) + 1.5) & \theta_e > 1 \end{cases} \quad (\text{C2})$$

(Svensson 1982; Esin et al. 1996). We assume temperatures are $T \gtrsim 10^5 \text{ K}$, which is in the small-angle uncertainty principle regime, so that $\bar{g}_{1,\text{ffei}} = (3k_b T_e / (\pi h\nu))^{1/2}$ for $h\nu / (k_b T) \gtrsim 1$ and $\bar{g}_{2,\text{ffei}} = (\sqrt{3}/\pi) \ln(2.2k_b T_e / (h\nu))$ for $h\nu / (k_b T) < 1$, which we interpolate as $\bar{g}_{\text{ffei}} = \bar{g}_{1,\text{ffei}} \exp(-1/x_e) + \bar{g}_{2,\text{ffei}} (1 - \exp(-1/x_e))$. More accurate analytical fitting formulae can be used (Svensson 1984; Shu 1991; Itoh et al. 2000; Sakamoto et al. 2001), although this level of accuracy is not required.

For abundances with mass fractions of Hydrogen, Helium, and ‘‘metals’’, respectively, *X*, *Y*, and *Z*, in a mostly ionized gas $n_e/\rho = 1/(\mu_e m_u) = (1 + X)/(2m_u)$ while $\sum_i n_i Z_i^2 = (\rho/m_u) \sum_i (X_i Z_i^2 / A_i) = (\rho/m_u)(X + Y + B)$ for mass fraction of species *i* of X_i , where $B = \sum_{i>2} (X_i Z_i^2 / A_i)$ with $X + Y + B \approx 1 - Z$ for $B \ll \{X, Y\}$. We often assume solar abundances (mass fractions of Hydrogen, Helium, and ‘‘metals’’, respectively, $X = 0.7$, $Y = 0.28$, $Z = 0.02$) with electron fraction $Y_e = (1 + X)/2$ giving mean molecular weight $\bar{\mu} \approx 1/(2X + 0.75Y + 0.5Z) \approx 0.62$ for ionized gas, which enters the gas entropy, pressure, and temperature T_g .

For free-free, $\kappa_{\text{ffei}} \approx 1 \times 10^{24} \rho^2 T_e^{-7/2} (1 + X)(1 - Z) R(\theta_e)$, for near solar abundances for the Planck mean. A Rosseland mean gives $\kappa_{\text{ffei,R}} \approx 3.8 \times 10^{22} \rho^2 T_e^{-7/2} (1 + X)(1 - Z) R(\theta_e)$, which is about 30 times smaller than the Planck mean. These calculations correct the formulae used in McKinney et al. (2015), where the free-free and free-bound coefficients were for Rosseland while the functional form was for Planck.

One can then compute the energy and number absorption mean from $\alpha_\nu^{\text{ffei}} = J_\nu^{\text{ffei}} / B_\nu(T_e)$ from Kirchoff’s law with a distribution based upon $T = T_e$.

C1 Razin Effect for Bremsstrahlung

The well-known infrared divergence for free-free leads to a formally infinite number of photons generated. Without any adjustment, the number absorption mean opacity diverges (Ascoli & Bussetti 1956; Yennie et al. 1961). For a given experiment size, this

divergence can be removed by adding in other non-bremsstrahlung processes that cannot be distinguished and that can occur (Akhiezer & Berestetsky 1953; Kaku 1993). The divergence is logarithmic, so any physical effect that would limit the presence of low frequency radiation would likely lead to a sufficient removal of the divergence to order unity or so.

Several processes can destroy the coherence of the emission process over the formation length while the electron and photon continue to distinguish themselves quantum mechanically. This includes Comptonization, Razin-type collective plasma effects (see below), finite temperature effects (Weldon 1994), Debye-length limit of the Coulomb potential (Gould 1990), and Landau-Pomeranchuk-Migdal (LPM) effect of multiple scatterings (Akopyan & Tsytovich 1976; Chen & Klein 1993; Shul’Ga & Fomin 1998; Klein 1999, 1997; Fortmann et al. 2005; Fortmann et al. 2007).

Collective plasma effects at the plasma frequency scale lead to dielectric suppression of the thermal bremsstrahlung rate that is the lowest frequency and strongest cut-off of radiation compared to the LPM or other effects (Scheuer 1960; Dawson & Oberman 1962; Mercier 1964; Bekefi 1966; Ichimaru 1973; Melrose 1972; Weldon 1994; Anthony et al. 1996). This can be accurately represented by multiplicative suppression factor of $S = \omega^2 / (\omega^2 + \omega_{pe}^2) = (1 + \omega_{pe}^2 / \omega^2)^{-1}$ (Melrose 1972) for electron plasma frequency ω_{pe} . As a contribution to the mean opacity, a sufficiently accurate suppression factor is given by

$$S = (1 - \omega_{pe}^2 / \omega^2)^{1/2} = S = (1 - x_p / x^2)^{1/2}, \quad (\text{C3})$$

(Bekefi 1966), for which the frequency integrals then start at $\omega = \omega_{pe}$ where $x_p = h\nu_{pe} / (k_b T_e)$ and $\nu_{pe} = \omega_{pe} / (2\pi)$ such that

$$x_p = 4.3 \times 10^{-7} \sqrt{n_e} / T_e = 3.3 \times 10^5 \sqrt{Y_e \rho / \bar{\mu}} / T_e. \quad (\text{C4})$$

So *S* can be treated as a suppression factor that simply depends upon the integral’s lower cut-off, here x_p . Note that this suppression is not an absorption process, and instead the light wave is evanescent below plasma frequencies. This cut-off operates even when the system is not in equilibrium. In principle, this means we need to tabulate/fit our opacities vs. the dimensionless lower frequency cut-off $x_{\text{cut}} = x_p$. Instead, for a given system, because the effect of the cut-off is logarithmic, we use a fixed cut-off for expected densities and temperatures.

C2 Tabulating/Fitting the Free-Free mean opacity

After substituting $\nu \rightarrow x k_b T_e / h$ and using x , $e^{-\xi}$, and $\zeta = T_\gamma / T_e$ as independent variables, and given a dimensionfull term set as

$$f(n_e, n_i, T_e) \equiv 1.2 \times 10^{24} T_e^{-7/2} \rho^2 (1 + X)(1 - Z) R(\theta_e), \quad (\text{C5})$$

then one can tabulate/fit the residual dimensionless factor $\kappa_{a,\text{ffei}} / f(n_e, n_i, T_e)$. The mean opacity is quite linear in log-log space, so such a direct look-up table can be generated of small dimensions that covers all dimensionless space of $\zeta = 10^{-10} - 10^{10}$ and $0 \leq e^{-\xi} \leq 1$.

For HARMRAD, we obtain a fitting function

$$\frac{\kappa_{a,\text{ffei}}}{f(n_e, n_i, T_e)} = a \zeta^{-b} \ln(1 + c \zeta), \quad (\text{C6})$$

where in general $a(e^{-\xi})$, $b(e^{-\xi})$, $c(e^{-\xi})$ are functions fitted for in that separate dimension. Similarly, the residual for the number opacity $\kappa_{an,\text{ffei}} / f(n_e, n_i, T_e)$ can be fitted with the same form of the expression with different constants.

The final fitted constants a, b, c for the energy opacity are

$$\begin{aligned} a &= 0.188(e^{-\xi})^{13.9} - 0.2(1 - (e^{-\xi}))^{0.565} + 0.356 \\ b &= 0.0722(e^{-\xi})^{1.36} + 0.255(1 - (e^{-\xi}))^{0.313} + 3.06 \\ c &= -1.41(e^{-\xi})^{3.08} - 1.44(1 - (e^{-\xi}))^{0.128} + 5.99 \end{aligned} \quad (C7)$$

and the constants a_n, b_n, c_n for the number opacity are

$$\begin{aligned} a_n &= 21.(e^{-\xi})^5 - 2.06(1 - (e^{-\xi}))^1 + 4. \\ b_n &= -0.412(e^{-\xi})^{59.1} + 0.000894(1 - (e^{-\xi}))^{10.2} + 3.15 \\ c_n &= 5.27(e^{-\xi})^{69.2} + 2.39(1 - (e^{-\xi}))^{0.552} \end{aligned} \quad (C8)$$

These fits use Razin and modified BE distribution based upon densities and temperatures for an Eddington-accreting BH X-ray binary. This gives a fit accurate for the energy opacity to less than 20% relative error for $10^{-5} < \zeta < 10^5$ and $0 < e^{-\xi} < 1$ with careful attention near $e^{-\xi} = 1$ where significant changes occur. The number opacity has a similar error except at $e^{-\xi} = 1$ where the results are accurate to factors of two as related to sharp changes right at $e^{-\xi} = 1$ for $\zeta \gtrsim 10^4$. The fitting coefficients at only $e^{-\xi} = 1$ are $\{a, b, c\} = \{0.532, 3.14, 4.52\}$ for the energy opacity and $\{a_n, b_n, c_n\} = \{20.0, 2.67, 5.00\}$ for the number opacity. These Planck coefficients can be used for the emission mean opacity when one also enforces $\zeta = 1$.

C3 Electron-Electron Opacity

The electron-electron opacity is the same as the electron-ion opacity except $(n_- + n_+)n_i$ is replaced by $(n_-^2 + n_+^2) \approx n_e^2$ and R_{ei} is replaced by

$$R_{ee}(\theta_e) = \begin{cases} 1.7\theta_e(1 + 1.1\theta_e + \theta_e^2 - 1.06\theta_e^{2.5}) & \theta_e \leq 1 \\ 1.7\theta_e^{0.5}(1.46(1.28 + \ln(1.12\theta_e))) & \theta_e > 1 \end{cases} \quad (C9)$$

(Esin et al. 1996). When obtaining mean opacities and emission rates, the density and R factors pull out and so any integrations apply to both these rates. This electron-electron opacity is added to the electron-ion opacity to give the final free-free opacity of

$$\kappa_{ff} = \kappa_{ffei} + \kappa_{ffee}, \quad (C10)$$

for both energy and number mean opacities.

C4 Effective Opacity including Lower temperature opacities

The bound-free (number and energy) opacity κ_{bf} is the same as free-free with $(1+X)(1-Z)$ replaced by $\sim 750Z(1+X+0.75Y)$ (Rybicki & Lightman 1986), where the $1+X+0.75Y$ term is roughly accurate near solar abundances. This assumes mostly ionized hydrogen and helium. One should also drop the high-temperature $R(\theta_e)$ factor.

Rosseland means are often provided for lower temperature opacities due to the expectation of applications to stellar interiors with temperature transport as the primary study. These opacities also tend to assume $T_e = T_\gamma$. Direct integration to obtain absorption means is not easy because the required frequency-dependent opacity data is not readily available.

To approximately convert published Rosseland means that assume $T_e = T_\gamma$ to absorption means that allow $T_e \neq T_\gamma$, we remove the electron scattering opacity (if it was included) and assume the opacity has a generic free-free-like form of $\alpha_x \times (1 - \exp(-x))/x^3$. This allows us to obtain the generic ratio of absorption mean to Rosseland mean of ~ 30 at $T_e = T_\gamma$ as consistent with the free-free calculations above, and this factor of 30 already appears in the below opacities.

At intermediate temperatures of 10^5 – 10^7 K and low densities, the free-free and bound-free opacity change their behavior for solar abundances to become the ‘‘Chianti opacity’’ of

$$\kappa_{\text{Chianti}}/\rho \sim 30 \times 10^{33} \rho (0.1 + Z/Z_{\text{solar}}) X(1 + X) T_e^{-4.7}. \quad (C11)$$

This behaves similarly to the free-free or free-bound opacity, but with a steeper temperature dependence. This accounts for the assumed $Z = Z_{\text{solar}} = 0.02$ for figure 34.1 in Draine (2011), most applicable for baryon densities of $n_b \sim 1 \text{ cm}^{-3}$. This gives a kink in the opacity at $T \sim 10^7$ K. To capture the drop in opacity at even lower temperatures and obtain a peak opacity at $T \sim 10^5$ K for solar abundances as in that figure 34.1, we use the H^- opacity of

$$\kappa_{H^-}/\rho \approx 33 \times 10^{-25} Z^{0.5} \rho^{0.5} T_g^{7.7}, \quad (C12)$$

and use the molecular opacity of $\kappa_m/\rho \approx 3Z$. The H^- and molecular opacity should have a absorption mean that will change with T_γ (e.g. Malygin et al. 2014), but in our case these low temperature opacities most often occur when $T_\gamma \sim T_e$.

The Chianti opacity works for low densities at intermediate temperatures, but at higher densities and lower temperatures additional effects modify the opacity. Realistic opacities for $T \lesssim 10^7$ K at higher densities can be obtained from the OPAL opacity tables that includes bound-bound lines and other physics (Iglesias & Rogers 1996). Other opacity calculations focused on stellar atmospheres give similar results (Seaton et al. 1994), while modern opacity tables use the OPAL opacity tables in some regimes (Paxton et al. 2011). Particularly, the opacity is enhanced between $T \sim 10^4$ K and $T \sim 10^5$ K at high densities due to H and He as well as enhanced around 10^5 K at low densities due to metals such like Fe. Such opacities have been approximately fit by Iben (1975) with corrections for the OPAL opacities by Guzik & Cox (1995), but those fits do not capture the low temperature or Fe line features. For $T \sim 10^5$ K, this opacity is significantly enhanced beyond the electron scattering opacity and can introduce driving of winds (Proga et al. 1998). We obtain a rough fit to the OPAL opacity Table 73 relevant for solar abundances. We subtract out the electron scattering opacity from their Rosseland mean to obtain a Rosseland absorption mean. The ‘‘OPAL opacity’’ fit is given as extra terms

$$\kappa_{\text{COPAL}} \sim 3 \times 10^{-13} \kappa_{\text{Chianti}} T_e^{1.6} \rho^{-0.4} \quad (C13)$$

and

$$\kappa_{\text{HOPAL}} \sim 10^4 T_g^{-1.2} \kappa_{H^-}. \quad (C14)$$

The Fe line at $T \approx 1.5 \times 10^5$ K can be approximated by adding (to the overall opacity) the Gaussian

$$\kappa_{\text{Fe}}/\rho \sim 0.3 \left(\frac{Z}{Z_{\text{solar}}} \right) e^{-6(-12 + \ln(T_g))^2}. \quad (C15)$$

This gives an iron line bump, which can affect the structure of disks and stars with substantial metals (Jiang et al. 2015, 2016). For the Fe line we do not modify this Rosseland mean into a Planck mean, because the line sits at a narrow band of frequencies and does not follow the free-free frequency dependence.

Our conversion from Rosseland to absorption means assuming the frequency-dependence is roughly free-free-like also allows us to apply the general free-free ζ dependence to these opacities as well estimate the energy and number mean opacities. We take the ratio of a given low-temperature κ (that applies to $T_e = T_\gamma$) to κ^{ff} at $\zeta = 1$, and then we set the final lower-temperature opacity as κ_{ff} times that ratio. This is done for both energy and number mean

opacities separately. Only for the temperature-independent molecular opacity and narrow-band Fe line opacity do we assume a ζ -independent opacity that is the same for number and energy mean opacities.

The final effective opacity κ_{eff} that bridges between the various opacities is given by

$$(\kappa_{\text{eff}} - \kappa_{\text{Fe}})^{-1} \sim (\kappa_{\text{m}} + \kappa_{\text{HOPAL}})^{-1} + \kappa_{\text{COPAL}}^{-1} + (\kappa_{\text{Chianti}} + \kappa_{\text{ff}} + \kappa_{\text{bf}})^{-1}. \quad (\text{C16})$$

This gives a fit to the "OPAL" opacities that is accurate to less than 30% in most cases and factors of ten for $T \ll 10^5 \text{K}$. This defines both the energy opacity and number opacity by assuming κ_{m} , κ_{HOPAL} , κ_{COPAL} , and κ_{Chianti} scale with free-free (and bound-free) for energy and number opacities.

APPENDIX D: CYCLO-SYNCHROTRON EMISSION

Cyclo-synchrotron is important when magnetic fields are strong in diffuse plasmas. We follow the discussion in Mahadevan et al. (1996) (see also Ginzburg & Syrovatskii 1965), where fits are given to cyclo-synchrotron at several discrete temperatures from $5 \times 10^8 \text{K}$ to $3.2 \times 10^{10} \text{K}$ as well as the ultrarelativistic limit. Other fits are considered for higher temperatures in Leung et al. (2011). Planck mean opacities have been considered before in the context of black hole accretion flows (Mason & Turolla 1992).

We consider thermal electrons with temperature T_e . Following Mahadevan et al. (1996) and Esin et al. (1996), the emissivity is

$$j_{\text{syn}}(\nu) = 4.43 \times 10^{-30} \nu_M n_e \frac{x_M I'(x_M)}{K_2(1/\theta_e)} d\nu \text{ erg cm}^{-3} \text{ s}^{-1}, \quad (\text{D1})$$

where $\theta_e = k_b T_e / (m_e c^2)$ and

$$x_M = \frac{\nu}{\nu_M}, \quad \nu_M = \frac{3}{2} \frac{eB}{2\pi m_e c} \theta_e^2 = 1.19 \times 10^7 B T_{10}^2 \text{ Hz}, \quad (\text{D2})$$

where $T_{10} = T_e / 10^{10} \text{K}$. The function $I'(x_M)$ is defined in Mahadevan et al. (1996), who provide the following fitting function for it,

$$I'(x_M) = \frac{4.0505\alpha}{x_M^{1/6}} \left(1 + \frac{0.40\beta}{x_M^{1/4}} + \frac{0.5316\gamma}{x_M^{1/2}} \right) \exp(-1.8899x_M^{1/3}). \quad (\text{D3})$$

In the ultrarelativistic limit $\alpha = \beta = \gamma = 1$ and $K_2(1/\theta_e) \rightarrow 2\theta_e^2$, while table 1 in Mahadevan et al. (1996) gives these coefficients for several other temperatures.

For synchrotron, a primary limitation of our opacities is the lack of non-thermal electrons, which would greatly modify the opacity in optically thin regions.

We use the low-frequency ($h\nu \ll kT_e$) (e.g. Rayleigh-Jeans for Planck) expansion for the distribution that appears in Kirchhoff's law within the opacity. Equivalently, we assume synchrotron emission at $h\nu \gtrsim k_b T_e$ is sub-dominant. This approximation is reasonable when $(kT_e)/(h\nu_M) \gg 1$, which will be valid for simulations we consider. One can then compute the energy and number absorption mean from $\alpha_{\nu}^{\text{syn}} = J_{\nu}^{\text{syn}}/B_{\nu}(T_e)$.

D1 Razin Effect for Synchrotron

Collective plasma effects, like the Razin effect, occur for synchrotron (Hornby & Williams 1966; McCray 1967; Simon 1969). This has been applied in the astrophysical case recently by Dougherty et al. (2003). The characteristic cut-off occurs at

$$\nu_R \approx \nu_{pe}^2 / \nu_B \approx 19 n_e / B. \quad (\text{D4})$$

or in terms of our dimensionless synchrotron integration variable in $x_M^{1/3} \sim 0.01(n_e/B)^{1/3}$. Below ν_R the synchrotron spectrum varies as $\nu^{3/2} \exp(-\nu_r/\nu)$ independent of the electron spectrum as long as there is no high-energy cut-off in the electron spectrum (in which case the ν_R is even higher at $\nu_R \approx 500\gamma_1 n_e^{3/4}/B^{1/2}$ for electron energy cut-off at $E = \gamma_1 m_e c^2$). This cut-off can be approximated quite accurately by multiplying $\alpha_{\nu}^{\text{syn}}$ by $e^{-\nu_r/\nu} = e^{-x_M/x}$ (Dougherty et al. 2003), which is the approximation we apply to our integrals. Like with free-free, the cut-off is small enough that changes in the dependence of opacity vs. $\zeta = T_e/T_e$ only occur for $\zeta \ll 1$, where the BE assumption is unlikely accurate and the simulation very rarely accesses. Hence, like with free-free, we only tabulate/fit the region above this change in character.

D2 Tabulating/Fitting Cyclo-Synchrotron

Defining

$$\phi \equiv \frac{kT_e}{h\nu_M}, \quad (\text{D5})$$

and using a dimensionfull factor of

$$g(n_e, B, T_e) = 5.85374 \times 10^{-14} n_e \phi \theta_e^{-3} T_e^{-1}, \quad (\text{D6})$$

the residual factor $\kappa_{\text{a,syn}}/g(n_e, B, T_e)$ and $\kappa_{\text{an,syn}}/g(n_e, B, T_e)$ can be tabulated. This residual is quite linear in log-log space, so not much resolution is required. In order to handle regions with weak or zero magnetic field strengths or radiation temperatures, we limit ϕ to no smaller than 10^{-20} and no larger than 10^{20} .

For HARMRAD, we fit the energy and number opacity residual by

$$\left(\frac{\kappa_{[\text{a,an},\text{syn}]}}{g(n_e, B, T_e)} \right)^{-1} \approx (a\phi^{-b} \ln(1+c\phi))^{-1} + (d\phi^{-e})^{-1} \quad (\text{D7})$$

with different coefficients a, b, c, d, e for the energy and number opacities. As with the free-free opacity, a, b, c, d, e are independently fitted for as functions of ϕ for each $e^{-\xi}$. We obtain fits are accurate to less than 20% relative error for any temperature T_e case given in Mahadevan et al. (1996) over the range $10^{-8} < \phi < 10^{15}$ and $0 \leq e^{-\xi} \leq 1$.

For densities and temperatures relevant for SgrA*, which enters the Razin cut-off and modification of the BE distribution, the ultrarelativistic temperature limit has coefficients for the energy opacity of

$$\begin{aligned} a &= -0.0295(e^{-\xi})^{2.29} - 0.143(1 - (e^{-\xi}))^{0.251} + 0.236 \\ b &= 0.00977(e^{-\xi})^{730} + 0.0291(1 - (e^{-\xi}))^{0.48} + 2.58 \\ c &= 1.29(e^{-\xi})^{1.59} + 3.46(1 - (e^{-\xi}))^{0.234} + 2.15 \\ d &= -78.1(e^{-\xi})^{66} - 40.3(1 - (e^{-\xi}))^{0.899} + 87.4 \\ e &= 0.415(e^{-\xi})^{0.399} + 1.04(1 - (e^{-\xi}))^{0.252} + 2.68 \end{aligned} \quad (\text{D8})$$

and the constants for the number opacity are

$$\begin{aligned} a_n &= 10.8(e^{-\xi})^{172} - 20.4(1 - (e^{-\xi}))^{0.699} + 29.2 \\ b_n &= -0.18(e^{-\xi})^{31.9} + 0.425(1 - (e^{-\xi}))^{0.179} + 2.76 \\ c_n &= 0.0207(e^{-\xi})^{9.69} + 0.0506(1 - (e^{-\xi}))^{0.804} + 0.0314 \\ d_n &= (1.51 \times 10^6)(e^{-\xi})^{2830} - 1.4 \times 10^5(1 - (e^{-\xi}))^{3.06 \times 10^{-12}} + 1.4 \times 10^5 \\ e_n &= 0.1(e^{-\xi})^{1.95} + 1.57(1 - (e^{-\xi}))^{0.124} \end{aligned} \quad (\text{D9})$$

These fits are accurate to 20% error over most of the domain $10^{-4} \leq \phi \leq 10^{15}$ and $0 \leq e^{-\xi} \leq 1$. For $e^{-\xi} = 1$, the coefficients for the energy opacity are $\{a, b, c, d, e\} =$

{0.206, 2.59, 3.44, 9.33, 3.09} and for the number opacity are $\{a_n, b_n, c_n, d_n, e_n\} = \{40.0, 2.58, 0.0522, 1.65 \times 10^6, 0.100\}$. These Planck coefficients can be used for the emission mean opacity when one also enforces $\phi \rightarrow (kT_e)/(h\nu_M)$. For $\phi \leq 10^{-5}$ these opacities becomes constant for each $e^{-\xi}$ vs. ϕ due to the Razin cut-off, so for such values of ϕ one should replace the opacities with their values at $\phi = 10^{-5}$ thus overriding the above fits.

For densities and temperatures relevant for an Eddington-accreting BH X-ray binary, we only obtain fitting accurate to order unity since other processes usually dominate and finding fitting functions can be difficult. The ultrarelativistic temperature limit has coefficients for the energy opacity of

$$\begin{aligned} a &= (-2.31 \times 10^{-8})(e^{-\xi})^{34} - (8.24 \times 10^{-9})(1 - (e^{-\xi}))^{2.42} + 1.27 \\ b &= -0.0261(e^{-\xi})^{738} - 0.00475(1 - (e^{-\xi}))^{1.55} + 1.06 \quad (\text{D10}) \\ c &= 0.000179(e^{-\xi})^{432} + 0.0000411(1 - (e^{-\xi}))^{0.372} + 0.000584 \\ d &= -17.7(e^{-\xi})^{49.4} - 3.33(1 - (e^{-\xi}))^{2.76} + 18.3 \\ e &= 0.427(e^{-\xi})^{0.654} + 1.23(1 - (e^{-\xi}))^{0.214} + 2.49 \end{aligned}$$

and the constants for the number opacity are

$$\begin{aligned} a_n &= -0.000359(e^{-\xi})^{1.31} - 0.000552(1 - (e^{-\xi}))^{0.135} + 0.00209 \\ b_n &= 0.035(e^{-\xi})^{5.43} + 0.0433(1 - (e^{-\xi}))^{0.159} + 0.948 \quad (\text{D11}) \\ c_n &= -0.122(e^{-\xi})^{37.1} - 0.0685(1 - (e^{-\xi}))^{2.8} + 1.04 \\ d_n &= -8.59(e^{-\xi})^{155} - 6.47(1 - (e^{-\xi}))^{0.436} + 8.71 \\ e_n &= -0.447(e^{-\xi})^{394} + 0.506(1 - (e^{-\xi}))^{0.155} + 2.45 \end{aligned}$$

For $e^{-\xi} = 1$, the coefficients for the energy opacity are $\{a, b, c, d, e\} = \{1.27, 1.03, 0.000763, 0.616, 2.91\}$ and for the number opacity are $\{a_n, b_n, c_n, d_n, e_n\} = \{0.00173, 0.983, 0.921, 0.123, 2.00\}$, to which the fits reduce to in this limit. These Planck coefficients can be used for the emission mean opacity when one also enforces $\phi \rightarrow (kT_e)/(h\nu_M)$.

For the temperatures down to $T = 10^8$ K described in Mahadevan et al. (1996), we have fitted the ratio of the discrete temperature mean opacities to the ultrarelativistic mean opacity. However, even at this lower temperature regime the fits by Mahadevan et al. (1996) are not broad-band enough to obtain an accurate mean opacity. Further, the simulations reach to much lower temperatures where there are no accurate fits. The fits are not too dissimilar from the ultrarelativistic mean opacities, except when ϕ is far from unity. So, we assume the ultrarelativistic opacity in all temperature regimes, as has been done by others (Fragile & Meier 2009). In the future, we can use more accurate cyclo-synchrotron calculations (Leung et al. 2011; Pandya et al. 2016) to compute the mean opacities.

APPENDIX E: COMPTON SCATTERING

Comptonization modifies the spectra and cools accretion flows (Kawashima et al. 2009; Schnittman et al. 2013; Xie et al. 2010; Kawashima et al. 2012), and Comptonization may generate useful observational signatures of super-Eddington accretion (Sutton et al. 2013). So it is an important process to consider.

E1 Thomson Scattering with Klein-Nishina

The electron scattering opacity is

$$\kappa_s \approx \kappa_{es}\kappa_{kn}, \quad (\text{E1})$$

where the Klein-Nishina (KN) correction for thermal electrons is $\kappa_{kn} \approx (1 + (T_e/(4.5 \times 10^8))^{0.86})^{-1}$ (Buchler & Yueh 1976) and

$\kappa_{es} = 0.2(1+X)$. This is applicable as a Rosseland mean for a Planck distribution of photons in non-degenerate matter (with KN correction applicable when $T_e \sim T_\gamma$). However, the Rosseland mean and streaming limit of the flux mean are similar to within 10% (Poutanen 2016), so a fixed scattering opacity as a function of optical depth is reasonable. A Wien distribution leads to a faster drop in scattering opacity as $\theta_e > 1$ (Svensson 1984), but this is a small correction as we do not end up with solutions having large regions with $\theta_e > 1$ or $\theta_\gamma > 1$.

E2 Thermal Comptonization via Kompaneets Scattering

We account for energy exchange via Comptonization in the soft-photon limit of Kompaneets equation, which we implement in a similar way to that described in Kawashima et al. (2009). For a general temperature, using the result given in equation (2.43) in Pozdnyakov et al. (1983), Sądowski et al. (2015) obtained a thermal Comptonization term of

$$\begin{aligned} \lambda_c &= -c\kappa_{es}E \left[\frac{4k(T_e - T_\gamma)}{m_e c^2} \right] \times \quad (\text{E2}) \\ &\times \left[1 + 3.683 \left(\frac{kT_e}{m_e c^2} \right) + 4 \left(\frac{kT_e}{m_e c^2} \right)^2 \right] \left[1 + \left(\frac{kT_e}{m_e c^2} \right) \right]^{-1}, \end{aligned}$$

which is consistent with the frequency-integrated energy-weighted Kompaneets equation and is valid for a BE distribution with any chemical potential. We assume that the Compton-scattered radiation is emitted isotropically in the fluid frame, which is a good approximation in the soft photon limit or for when there are numerous scatterings.

This scheme is tested for accuracy as in Ryan et al. (2015) section 4.2, except they started with a delta function for the photon distribution and evolved the photons in a scattering region to see the redistribution toward Wien. Since we assume Bose-Einstein, we start with Planck at $T_\gamma = 500061$ K that gives their energy density for our Planck initial distribution. We assume their $T_e = 5 \times 10^7$ K, baryon number density $n_b = 2.5 \times 10^{17}$, and ideal gas constant $\gamma = 5/3$. Then, we evolve the system and check the timescale for equilibration as well as the final distribution and temperature, which can be computed from the conditions of thermal equilibrium and photon conservation. Analytically we obtain a final temperature of $T \approx 2.778 \times 10^6$ K and $e^{-\xi} = 0.0070$. We use harmrad and evolve for $t = 20$ s. If we evolve for this time in a single timestep, as possible with our implicit method, we find that after this time, $T_e \approx 2.786 \times 10^6$ K, $T_\gamma \approx 2.779 \times 10^6$ K, and $e^{-\xi} \approx 0.0070$ (i.e. quite Wien). If we evolve the system for about 48,000 timesteps, then we find $T_e = T_\gamma \approx 2.779 \times 10^6$ K (with temperatures similar to machine precision) and $e^{-\xi} \approx 0.0070$. In this case, the temperatures approach each other on a timescale of 0.02s, as is the equilibration timescale. Errors in these results are dominated by the temperature and chemical potential fits for the BE distribution that are only accurate to at worst 2% as well as by the first order time error in the implicit method when taking only a single large timestep.

Other extensions to Kompaneets can be found elsewhere that account for relativistic effects (Sazonov & Sunyaev 1998; Challinor & Lasenby 1998; Nagirner et al. 1997; Challinor & Lasenby 1998; Brown & Preston 2012; Nozawa & Kohyama 2015), high temperatures (Sampson 1959; Xie et al. 2010; Garain & Chakrabarti 2013; Niedzwiecki et al. 2014), and evolve the electron temperature (Procopio & Burigana 2009; Chluba & Sunyaev 2012).

E3 Double Compton

An important source of soft photons is the double (or radiative) Compton effect, which dominates bremsstrahlung in radiation-dominated diffuse plasmas (Lightman 1981; Thorne 1981; Svensson 1984; Chluba et al. 2007). These photons are therefore an important source for thermal Comptonization.

The statistical factor for the DC emission process, $e + \gamma_0 \leftrightarrow e' + \gamma_1 + \gamma_2$, is given by

$$\begin{aligned} F &= f(E) n_0(1+n_1)(1+n_2) - f(E') n_1 n_2(1+n_0) \\ &= f(E) n_0(1+n_1) \left[(1+n_2) - e^{-E'/kT_e} \frac{(1+n_0)}{n_0} \frac{n_1}{(1+n_1)} n_2 \right] \end{aligned} \quad (\text{E3})$$

where a relativistic Maxwell-Boltzmann, $f(E) \propto e^{-E/kT_e}$, was assumed for the electrons. Inserting BE distributions for the photons around energies $h\nu_0$ and $h\nu_1$ and using $E' - E = h(\nu_0 - \nu_1 - \nu_2)$, one has

$$\begin{aligned} F &= f(E) n_0(1+n_1) \left[(1+n_2) - e^{\frac{h(\nu_1+\nu_2-\nu_0)}{kT_e}} e^{x_0+\mu_0} e^{-x_1-\mu_1} n_2 \right] \\ &= f(E) n_0(1+n_1) \left[(1+n_2) - e^{\Delta x \left(1 - \frac{T_\gamma}{T_e}\right)} e^{x_2} n_2 \right], \end{aligned} \quad (\text{E4})$$

where in the last step we assumed constant chemical potential, $\mu_1 = \mu_0$. Let's look at the average change in the energy of the photon

$$\Delta x = x_0 - x_1 - x_2. \quad (\text{E5})$$

In the approximations that are used for the derivations, in fact, there is no direct energy exchange, so that all the energy comes from the scattering photons and $x_0 - x_1 - x_2 \approx 0$. Thus, we have

$$\begin{aligned} F &\approx f(E) n_0(1+n_1) [(1+n_2) - e^{x_2} n_2] \\ &= f(E) n_0(1+n_1) [1 - n_2(e^{x_2} - 1)]. \end{aligned} \quad (\text{E6})$$

This shows that without direct energy exchange in the scattering event (no recoil and Doppler boosting), the spectrum is driven towards an equilibrium at the temperature of the photon field with $T = T_\gamma$. Energy exchange leads to a small correction to the Compton process for the high frequency photons (γ_0 and γ_1), which neglect here (for more discussion see Chluba 2005).

For photon occupation number n_x , the number density of photons is

$$n = (8\pi(k_b T_\gamma)^3 / (h^3 c^3)) \int_0^\infty n_x x^2 dx, \quad (\text{E7})$$

where here we set the dimensionless energy $x = h\nu / (k_b T_\gamma)$.

The change in the occupation number per unit time due to emission of double Compton photons with energy x is

$$\frac{dn_x^{\text{DC}}}{dt} = t_c^{-1} \frac{4\alpha}{3\pi} \theta_\gamma^2 \frac{1}{x^3} I_{\text{DC}} \quad (\text{E8})$$

(Lightman 1981; Chluba et al. 2007), where $\theta_\gamma \equiv k_b T_\gamma / (m_e c^2)$, $t_c^{-1} = n_e c \sigma_T = \kappa_{\text{es}} c$, and α is the fine structure constant. Notice that the double Compton rates are dependent upon the radiation temperature T_γ , unlike the other emission processes. Note that Lightman 1981 did not distinguish T_e from T_γ when obtaining their equation 10a, but their derivation only depends explicitly upon the radiation temperature and just assumed $\theta_e \ll 1$ in order to drop frequency

shift terms. The dimensionless DC emission-Gaunt factor is

$$I_{\text{DC}}(x, e^{-\xi}, \theta_e, \theta_\gamma) = \int_{2x}^\infty y^4 (1+n_{y-x}) n_y \left[\frac{x}{y} H_G \left(\frac{x}{y} \right) \right] G_m(y\theta_\gamma, \theta_e) dy, \quad (\text{E9})$$

where $y = h\nu / (k_b T_\gamma)$ is a dummy variable for x and n_{y-x} means to substitute $y-x$ as x in n_x , and dimensionless

$$G_m(x\theta_\gamma, \theta_e) = \int_0^\infty G_m(\omega_0, \beta_0) f(E_0, \theta_e) p_0^2 dp_0 \quad (\text{E10})$$

for momentum $p_0 = m_e \gamma_0 \beta_0$ and $\gamma_0 = 1 / \sqrt{1 - \beta_0^2}$, photon frequency per electron rest-mass energy $\omega_0 = h\nu_0 / (m_e c^2) = x\theta_\gamma$, 3-velocity β_0 , and energy $E_0 = m_e \gamma_0$ or $E_0^2 = p_0^2 + (m_e c^2)^2$. The relativistic Maxwell-Boltzmann distribution per n_e is

$$f(E, \theta_e) = \frac{1}{4\pi m_e^3 K_2(1/\theta_e) \theta_e} e^{-E/m_e \theta_e}, \quad (\text{E11})$$

where $K_2(1/\theta_e)$ is the modified Bessel function of the second kind, with $\theta_e = k_b T_e / (m_e c^2)$, and where n_e is the electron number density, such that $1 = \int f(E) d^3 p$, and

$$G_m(\omega_0, \beta_0) \approx \frac{\gamma_0^2 (1 + \beta_0^2)}{1 + \sum_{k=1}^4 f_k(\beta_0) \gamma_0^k \omega_0^k}, \quad (\text{E12a})$$

with the functions $f_k(\beta_0)$

$$f_1(\beta_0) = \frac{1}{1 + \beta_0^2} \left[\frac{21}{5} + \frac{42}{5} \beta_0^2 + \frac{21}{25} \beta_0^4 \right] \quad (\text{E12b})$$

$$f_2(\beta_0) = \frac{1}{(1 + \beta_0^2)^2} \left[\frac{84}{25} + \frac{217}{25} \beta_0^2 + \frac{1967}{125} \beta_0^4 \right] \quad (\text{E12c})$$

$$f_3(\beta_0) = -\frac{1}{(1 + \beta_0^2)^3} \left[\frac{2041}{875} + \frac{1306}{125} \beta_0^2 \right] \quad (\text{E12d})$$

$$f_4(\beta_0) = \frac{1}{(1 + \beta_0^2)^4} \frac{9663}{4375} \quad (\text{E12e})$$

(Chluba et al. 2007; Chluba & Sunyaev 2012) (with typo fixed in f_3). As compared to previous expressions that require $\theta_e \ll 1$ and $\theta_\gamma \ll 1$ and $x \ll 1$ (i.e. cold electrons, cold photons, and soft photons) (Lightman 1981) where $I_{\text{DC}} \rightarrow I_{0,\text{DC}}$ with

$$I_{0,\text{DC}} = \int_0^\infty x^4 (1+n_x) n_x dx, \quad (\text{E13})$$

our version from Chluba et al. (2007) is accurate for moderately relativistic electrons and photons (i.e. $\theta_e \lesssim 1$ and $\theta_\gamma \lesssim 1$ and $x \lesssim 1$). For $x \gtrsim 1$ double Compton is suppressed as e^{-2x} , and high energy photons are more readily generated by single Comptonization off the double Compton photons (Thorne 1981).

The differential number emission rate (number per unit time per unit volume) is

$$d\dot{n}_{\text{DC}} = (8\pi(k_b T_\gamma)^3 / (h^3 c^3)) x^2 dx \frac{dn_x^{\text{DC}}}{dt}, \quad (\text{E14})$$

and the differential emission rate (energy per unit time per unit volume) is

$$d\dot{E}_{\text{DC}} = (k_b T_\gamma) x d\dot{n}_{\text{DC}}, \quad (\text{E15})$$

such that

$$j_{\text{DC}}(x) = d\dot{E}_{\text{DC}} / (4\pi). \quad (\text{E16})$$

The energy and number mean opacities can then be computed from $\alpha_\nu^{\text{DC}} = j_\nu^{\text{DC}} / B_\nu(T_\gamma) = j^{\text{DC}}(x) / B(x, T_\gamma)$ where $B(x) =$

$B_\nu(d\nu/dx)$ with $d\nu/dx = k_B T_\gamma/h$. As shown in §E3, here Kirchhoff's law is based upon a distribution at $T = T_\gamma$, because these DC expressions include no recoil or Doppler shifting, and they presume energy balance between the incoming photon and the two outgoing photons. That is, DC here includes no energy exchange with electrons and so absorption only drives the photon distribution to Planck at its own radiation temperature. Energy exchange from single Comptonization dominates that one would obtain from recoil/Doppler for double Compton, so the energy exchange from Eq. (E2) is sufficient as a independent (non-DC) mechanism to drive thermal equilibrium between electrons and photons. Unlike free-free, electrons can be completely cold and DC emission still occurs if there are seed photons (Lightman 1981).

We are not aware of work done to establish the Razin effect with Double Compton, so we apply the same approach used for bremsstrahlung.

E4 Tabulating/Fitting Double Compton

The dimensionfull factor for the DC opacity is

$$h(n_e, T_\gamma, e^{-\xi}) = 7.360 \times 10^{-46} n_e T_\gamma^2 e^{-\xi} \quad (\text{E17})$$

where the $e^{-\xi}$ factor was pulled from the dimensionless integrals. Now the residual factor $\kappa_{a,DC}/(p(\theta_e)h(n_e, T_\gamma, e^{-\xi}))$ and $\kappa_{an,DC}/(p(\theta_e)h(n_e, T_\gamma, e^{-\xi}))$ can be tabulated. The DC emission opacity is obtained by choosing $T_{eq} = T_\gamma$ and $\mu_{eq} = 0$, but that still leaves the emission opacity dependent upon the radiation μ from the DC j_ν .

For HARMRAD, we fit the opacity residuals. For DC our approach is to first fit the regime $\theta_e \ll 1$ where the residual is constant vs. θ_e , and then find a rough fit vs. $\theta_e \gtrsim 0.01$ when the opacity begins to change by more than 20% vs. θ_e .

For any θ_e , the residual factors $\kappa_{a,DC}/(p(\theta_e)h(n_e, T_\gamma, e^{-\xi}))$ and $\kappa_{an,DC}/(p(\theta_e)h(n_e, T_\gamma, e^{-\xi}))$ can be fit by the form

$$\left(\frac{\kappa_{\{a,n\},DC}}{p(\theta_e)h(n_e, T_\gamma, e^{-\xi})} \right)^{-1} \approx a^{-1} + (b\theta_e^{-c})^{-1} + (d\theta_e^{-c/3})^{-1}, \quad (\text{E18})$$

with a relative error less than 20%. For DC, we choose densities and temperatures relevant for an Eddington-accreting BH X-ray binary, which enters the Razin cut-off and modification of the BE distribution. DC for diffuse systems like SgrA* is much lower than synchrotron due to the very low radiation temperature of thermal synchrotron, so it is not considered.

For $\theta_e \ll 1$, we obtain fits are accurate to less than 20% relative error for all $10^{-4} \leq \theta_\gamma \leq 10^2$ and $0 \leq e^{-\xi} \leq 1$. The energy absorption opacity coefficients are

$$\begin{aligned} a &= 4.16(1 - (e^{-\xi}))^{1.69} + 6.7(e^{-\xi})^{0.942} + 3.1 \times 10^{-8} \\ b &= -0.0334(1 - (e^{-\xi}))^{0.469} - 0.0021(e^{-\xi})^{0.0217} + 0.042 \\ c &= -0.18(e^{-\xi})^{33.3} + 0.201(1 - (e^{-\xi}))^{0.258} + 3.8 \\ d &= 0.0169(e^{-\xi})^{35.4} - 0.0626(1 - (e^{-\xi}))^{0.35} + 0.118 \end{aligned} \quad (\text{E19})$$

The energy emission opacity coefficients are

$$\begin{aligned} a &= -0.0589(1 - (e^{-\xi}))^{10.7} + 0.488(e^{-\xi})^{1.75} + 6.34 \\ b &= 0.0282(e^{-\xi})^{1.56} + 0.0142(1 - (e^{-\xi}))^{0.361} + 0.00875 \\ c &= -0.16(e^{-\xi})^{15.4} + 0.184(1 - (e^{-\xi}))^{0.366} + 3.78 \\ d &= 0.015(e^{-\xi})^{26.3} - 0.0256(1 - (e^{-\xi}))^{0.398} + 0.119 \end{aligned} \quad (\text{E20})$$

The Planck limit gives coefficients $\{a, b, c, d\} = \{6.83, 0.0374, 3.63, 0.134\}$ for the energy absorption and emission opacities.

The number absorption opacity coefficients are

$$\begin{aligned} a_n &= 29.4(e^{-\xi})^{285.} - 76.4(1 - (e^{-\xi}))^{0.136} + 87.5 \\ b_n &= 0.196(e^{-\xi})^{18.1} - 1.12(1 - (e^{-\xi}))^{0.134} + 1.16 \\ c_n &= 0.0427(1 - (e^{-\xi}))^{182.} - 0.8(e^{-\xi})^{21.6} + 3.93 \\ d_n &= 1.87(e^{-\xi})^{309.} - 2.72(1 - (e^{-\xi}))^{0.106} + 2.86 \end{aligned} \quad (\text{E21})$$

The number emission mean opacity coefficients are

$$\begin{aligned} a_n &= -81.7(e^{-\xi})^{1.01} - 94.8(1 - (e^{-\xi}))^{0.925} + 198. \\ b_n &= 1.31(e^{-\xi})^{1.12} + 1.05(1 - (e^{-\xi}))^{0.249} + 4.8 \times 10^{-11} \\ c_n &= -0.418(e^{-\xi})^{14.8} + 0.442(1 - (e^{-\xi}))^{0.361} + 3.44 \\ d_n &= 1.37(e^{-\xi})^{31.3} - 1.38(1 - (e^{-\xi}))^{0.316} + 3.38 \end{aligned} \quad (\text{E22})$$

The Planck limit gives coefficients $\{a_n, b_n, c_n, d_n\} = \{116., 1.34, 3.03, 4.72\}$.

To obtain a rough fit that will be accurate for $\theta_e \gtrsim 0.01$, we fit the ratio of the higher θ_e opacities to the $\theta_e \ll 1$ opacity. This gives a fit to the ratio $p(\theta_e)$ of the general opacity to the $\theta_e \ll 1$ opacity

$$p(\theta_e) \approx (1 + \theta_e)^{-3} \quad (\text{E23})$$

which does not change the accuracy at low θ_e but improves the accuracy for $\theta_e \leq 1$ to be within a factor of three or better and $\theta_e \leq 0.1$ to be within a factor of two or better. This factor $p(\theta_e)$ gives the same correction and accuracy for all opacities (energy absorption, number absorption, energy emission, and number emission). The DC calculation is only accurate for $\theta_e \leq 1$, beyond which pair production processes (not included) become important.

REFERENCES

- Abramowicz M. A., Czerny B., Lasota J. P., Szuszkiewicz E., 1988, ApJ, 332, 646
- Akhiezer A., Berestetsky V., 1953, Quantum electrodynamics, no. v. 1 in Quantum Electrodynamics, Technical information service extension [1953?]
- Akopyan A. V., Tsytoich V. N., 1976, Soviet Journal of Experimental and Theoretical Physics, 44, 87
- Anthony P. L., Becker-Szendy R., Bosted P. E., et al., 1996, Physical Review Letters, 76, 3550
- Ascoli R., Bussetti G., 1956, Il Nuovo Cimento, 4, 2, 189
- Avara M. J., McKinney J. C., Reynolds C. S., 2015, ArXiv e-prints
- Balbus S. A., Hawley J. F., 1998, Reviews of Modern Physics, 70, 1
- Bégué D., Pe'er A., 2015, ApJ, 802, 134
- Bekefi G., 1966, Radiation processes in plasmas, Wiley series in plasma physics, Wiley
- Blaes O. M., Davis S. W., Hirose S., Krolik J. H., Stone J. M., 2006, ApJ, 645, 1402
- Brown L. S., Preston D. L., 2012, Astroparticle Physics, 35, 742
- Buchler J. R., Yueh W. R., 1976, ApJ, 210, 440
- Burigana C., Danese L., de Zotti G., 1991, A&A, 246, 49
- Burigana C., de Zotti G., Danese L., 1995, A&A, 303, 323
- Castelló-Mor N., Netzer H., Kaspi S., 2016, MNRAS, 458, 1839
- Castor J. I., 2004, Radiation Hydrodynamics
- Challinor A., Lasenby A., 1998, ApJ, 499, 1
- Chen P., Klein S., 1993, AIP Conf.Proc., 279, 929
- Chluba J., 2005, Spectral Distortions of the Cosmic Microwave Background, Ph.D. thesis, LMU München
- Chluba J., 2014, MNRAS, 440, 2544
- Chluba J., Sazonov S. Y., Sunyaev R. A., 2007, A&A, 468, 785
- Chluba J., Sunyaev R. A., 2012, MNRAS, 419, 1294
- Christen T., Kassubek F., 2014, Journal of Physics D Applied Physics, 47, 363001
- Dai L., McKinney J. C., Miller M. C., 2015, ApJ, 812, L39

- Davis S. W., Jiang Y.-F., Stone J. M., Murray N., 2014, *ApJ*, 796, 107
- Dawson J., Oberman C., 1962, *Physics of Fluids (1958-1988)*, 5, 5, 517
- Di Matteo T., Celotti A., Fabian A. C., 1997, *MNRAS*, 291, 805
- Dougherty S. M., Pittard J. M., Kasian L., Coker R. F., Williams P. M., Lloyd H. M., 2003, *A&A*, 409, 217
- Draine B. T., 2011, *Physics of the Interstellar and Intergalactic Medium*
- Esin A. A., Narayan R., Ostriker E., Yi I., 1996, *ApJ*, 465, 312
- Fabian A. C., Lohfink A., Kara E., Parker M. L., Vasudevan R., Reynolds C. S., 2015, *MNRAS*, 451, 4375
- Fortmann C., Reinholz H., Roepke G., Wierling A., 2005, *ArXiv Physics e-prints*
- Fortmann C., Roepke G., Wierling A., 2007, in *Plasma Science, 2007. ICOPS 2007. IEEE 34th International Conference on*, 230–230
- Fragile P. C., Gillespie A., Monahan T., Rodriguez M., Anninos P., 2012, *ApJS*, 201, 9
- Fragile P. C., Meier D. L., 2009, *ApJ*, 693, 771
- Fragile P. C., Olejar A., Anninos P., 2014, *ApJ*, 796, 22
- Gammie C. F., 1999, *ApJ*, 522, L57
- Gammie C. F., McKinney J. C., Tóth G., 2003, *ApJ*, 589, 444
- Garain S. K., Chakrabarti H. G. S. K., 2013, *ArXiv e-prints*
- Ginzburg V. L., Syrovatskii S. I., 1965, *ARA&A*, 3, 297
- Gould R. J., 1990, *ApJ*, 362, 284
- Guzik J. A., Cox A. N., 1995, *ApJ*, 448, 905
- Heng K., Hayek W., Pont F., Sing D. K., 2012, *MNRAS*, 420, 20
- Hirose S., Krolik J. H., Blaes O., 2009, *ApJ*, 691, 16
- Hornby J. M., Williams P. J. S., 1966, *MNRAS*, 131, 237
- Hubeny I., Burrows A., Sudarsky D., 2003, *ApJ*, 594, 1011
- Huebner W., Barfield W., 2014, *Opacity, Astrophysics and Space Science Library*, Springer New York
- Iben Jr. I., 1975, *ApJ*, 196, 525
- Ichimaru S., 1973, *Basic Principles Of Plasma Physics: A Statistical Approach (Frontiers in Physics)*, *Frontiers in Physics*, W. A. Benjamin
- Iglesias C. A., Rogers F. J., 1996, *ApJ*, 464, 943
- Igumenshchev I. V., Narayan R., Abramowicz M. A., 2003, *ApJ*, 592, 1042
- Itoh N., Sakamoto T., Kusano S., Nozawa S., Kohyama Y., 2000, *ApJS*, 128, 125
- Jiang Y.-F., Cantiello M., Bildsten L., Quataert E., Blaes O., 2015, *ApJ*, 813, 74
- Jiang Y.-F., Davis S., Stone J., 2016, *ArXiv e-prints*
- Jiang Y.-F., Stone J. M., Davis S. W., 2013, *ApJ*, 778, 65
- Jiang Y.-F., Stone J. M., Davis S. W., 2014a, *ApJ*, 796, 106
- Jiang Y.-F., Stone J. M., Davis S. W., 2014b, *ApJ*, 784, 169
- Just D. W., Brandt W. N., Shemmer O., et al., 2007, *ApJ*, 665, 1004
- Kaku M., 1993, *Quantum Field Theory: A Modern Introduction*, Oxford University Press
- Kawashima T., et al., 2012, *ApJ*, 752, 18
- Kawashima T., Ohsuga K., Mineshige S., Heinzeller D., Takabe H., Matsumoto R., 2009, *PASJ*, 61, 769
- Klein S., 1999, *Reviews of Modern Physics*, 71, 1501
- Klein S. R., 1997, *NASA STI/Recon Technical Report N*, 99, 32370
- Kubota A., Done C., 2004, *MNRAS*, 353, 980
- Kulkarni A. K., Penna R. F., Shcherbakov R. V., et al., 2011, *MNRAS*, 414, 1183
- Leung P. K., Gammie C. F., Noble S. C., 2011, *ApJ*, 737, 21
- Lightman A. P., 1981, *ApJ*, 244, 392
- Ludwig H.-G., Jordan S., Steffen M., 1994, *A&A*, 284, 105
- Mahadevan R., Narayan R., Yi I., 1996, *ApJ*, 465, 327
- Malygin M. G., Kuiper R., Klahr H., Dullemond C. P., Henning T., 2014, *A&A*, 568, A91
- Mason A., Turolla R., 1992, *ApJ*, 400, 170
- McCray R., 1967, *ApJ*, 147, 544
- McKinney J. C., 2006, *MNRAS*, 368, 1561
- McKinney J. C., Blandford R. D., 2009, *MNRAS*, 394, L126
- McKinney J. C., Dai L., Avara M. J., 2015, *MNRAS*, 454, L6
- McKinney J. C., Gammie C. F., 2004, *ApJ*, 611, 977
- McKinney J. C., Tchekhovskoy A., Blandford R. D., 2012, *MNRAS*, 423, 3083
- McKinney J. C., Tchekhovskoy A., Sadowski A., Narayan R., 2014, *MNRAS*, 441, 3177
- McKinney J. C., Uzdensky D. A., 2012, *MNRAS*, 419, 573
- Melrose D. B., 1972, *Ap&SS*, 18, 267
- Mercier R. P., 1964, *Proceedings of the Physical Society*, 83, 5, 819
- Mihalas D., Mihalas B. W., 1984, *Foundations of radiation hydrodynamics*
- Miller M. C., Boutloukos S., Lo K. H., Lamb F. K., 2011, in *Fast X-ray Timing and Spectroscopy at Extreme Count Rates (HTRS 2011)*, 24
- Mishra B., Fragile P. C., Johnson L. C., Kluźniak W., 2016, *ArXiv e-prints*
- Modest M. F., ed., 2013, *Front matter*, Academic Press, Boston, third edition
- Nagirner D., Loskutov V., Grachev S., 1997, *Astrophysics*, 40, 3, 227
- Narayan R., Igumenshchev I. V., Abramowicz M. A., 2003, *PASJ*, 55, L69
- Narayan R., Zhu Y., Psaltis D., Sądowski A., 2016, *MNRAS*, 457, 608
- Niedzwiecki A., Stepnik A., Xie F.-G., 2014, *ArXiv e-prints*
- Novikov I. D., Thorne K. S., 1973, in *Black Holes (Les Astres Occlus)*, edited by C. Dewitt, B. S. Dewitt, 343–450
- Nozawa S., Kohyama Y., 2015, *Astroparticle Physics*, 62, 30
- O’ Riordan M., Pe’er A., McKinney J. C., 2016a, *ArXiv e-prints*
- O’ Riordan M., Pe’er A., McKinney J. C., 2016b, *ApJ*, 819, 95
- Page D. N., Thorne K. S., 1974, *ApJ*, 191, 499
- Pandya A., Zhang Z., Chandra M., Gammie C. F., 2016, *ApJ*, 822, 34
- Patch R., 1967, *J. Quant. Spec. Radiat. Transf.*, 7, 611
- Paxton B., Bildsten L., Dotter A., Herwig F., Lesaffre P., Timmes F., 2011, *ApJS*, 192, 3
- Penna R. F., McKinney J. C., Narayan R., Tchekhovskoy A., Shafee R., McClintock J. E., 2010, *MNRAS*, 408, 752
- Pessah M. E., Psaltis D., 2005, *ApJ*, 628, 879
- Poutanen J., 2016, *ArXiv e-prints*
- Poutanen J., Svensson R., 1996, *ApJ*, 470, 249
- Pozdnyakov L. A., Sobol I. M., Syunyaev R. A., 1983, *Astrophysics and Space Physics Reviews*, 2, 189
- Procopio P., Burigana C., 2009, *A&A*, 507, 1243
- Proga D., Stone J. M., Drew J. E., 1998, *MNRAS*, 295, 595
- Roberts L. F., Ott C. D., Haas R., O’Connor E. P., Diener P., Schnetter E., 2016, *ArXiv e-prints*
- Rosdahl J., Teyssier R., 2015, *MNRAS*, 449, 4380
- Ryan B. R., Dolence J. C., Gammie C. F., 2015, *ApJ*, 807, 31
- Rybicki G. B., Lightman A. P., 1986, *Radiative Processes in Astrophysics*
- Sadowski A., Narayan R., 2015a, *ArXiv e-prints*
- Sadowski A., Narayan R., 2015b, *arxiv: 1503.00654*
- Sadowski A., Wielgus M., Narayan R., Abarca D., McKinney J. C., 2016, *ArXiv e-prints*
- Sakamoto T., Itoh N., Kusano S., Nozawa S., Kohyama Y., 2001, in *New Century of X-ray Astronomy*, edited by H. Inoue, H. Kunieda, vol. 251 of *Astronomical Society of the Pacific Conference Series*, 268
- Sampson D., 1965, *J. Quant. Spec. Radiat. Transf.*, 5, 211
- Sampson D. H., 1959, *ApJ*, 129, 734
- Sazonov S. Y., Sunyaev R. A., 1998, *ApJ*, 508, 1
- Sądowski A., 2016, *MNRAS*, 459, 4397
- Sądowski A., Narayan R., McKinney J. C., Tchekhovskoy A., 2014, *MNRAS*, 439, 503
- Sądowski A., Narayan R., Tchekhovskoy A., Abarca D., Zhu Y., McKinney J. C., 2015, *MNRAS*, 447, 49
- Scheuer P. A. G., 1960, *MNRAS*, 120, 231
- Schnittman J. D., Krolik J. H., Noble S. C., 2013, *ApJ*, 769, 156
- Seaton M. J., 1993, *MNRAS*, 265, L25
- Seaton M. J., Yan Y., Mihalas D., Pradhan A. K., 1994, *MNRAS*, 266, 805
- Shu F. H., 1991, *The physics of astrophysics. Volume 1: Radiation*
- Shul’Ga N. F., Fomin S. P., 1998, *Soviet Journal of Experimental and Theoretical Physics*, 86, 32
- Simon M., 1969, *ApJ*, 156, 341
- Steffen A. T., Strateva I., Brandt W. N., et al., 2006, *AJ*, 131, 2826
- Struchtrup H., 1997, *Annals of Physics*, 257, 111
- Sturrock P. A., Holzer T. E., Mihalas D. M., Ulrich R. K., eds., 1986, *Physics of the sun. Volume 1 - The solar interior. Volume 2 The solar atmosphere. Volume 3 - Astrophysics and solar-terrestrial relations*, vol. 1
- Sunyaev R. A., Zeldovich Y. B., 1970, *Ap&SS*, 7, 3

- Sutton A. D., Roberts T. P., Middleton M. J., 2013, *MNRAS*, 435, 1758
Svensson R., 1982, *ApJ*, 258, 335
Svensson R., 1984, *MNRAS*, 209, 175
Takahashi H. R., Ohsuga K., Kawashima T., Sekiguchi Y., 2016, *ApJ*, 826, 23
Takahashi H. R., Ohsuga K., Sekiguchi Y., Inoue T., Tomida K., 2013, *ApJ*, 764, 122
Tchekhovskoy A., McKinney J. C., Narayan R., 2012, *Journal of Physics Conference Series*, 372, 1, 012040
Tchekhovskoy A., Narayan R., McKinney J. C., 2011, *MNRAS*, 418, L79
Thorne K. S., 1981, *MNRAS*, 194, 439
Tsang B. T.-H., Milosavljević M., 2015, *MNRAS*, 453, 1108
Uzdensky D. A., McKinney J. C., 2011, *Physics of Plasmas*, 18, 4, 042105
Vögler A., Bruls J. H. M. J., Schüssler M., 2004, *A&A*, 421, 741
Vurm I., Lyubarsky Y., Piran T., 2013, *ApJ*, 764, 143
Weldon H. A., 1994, *Phys. Rev. D*, 49, 1579
Xie F.-G., Niedźwiecki A., Zdziarski A. A., Yuan F., 2010, *MNRAS*, 403, 170
Yennie D. R., Frautschi S. C., Suura H., 1961, *Annals of Physics*, 13, 379